LUND UNIVERSITY

Tire Models for Use in Braking Applications

Svendenius, Jacob

2003

[Link to publication](#)

Total number of authors:
1

Department of Automatic Control Lund Institute of Technology Box 118 SE-221 00 Lund Sweden	*Document name* LICENTIATE THESIS
	Date of issue November 2003
	Document Number ISRN LUTFD2/TFRT--3232--SE

Author(s) Jacob Svendenius	*Supervisor* Björn Wittenmark Per Hagander Per-Axel Roth
	Sponsoring organisation Haldex Brake Products AB

Title and subtitle
Tire Models for Use in Braking Applications

Abstract

The tire is a significant part for control of a vehicle. For a well-working brake system the contact properties between the tire and the ground is the limiting factor for a safe braking. To get optimal performance it is important that the system can utilize all friction resources.

The brush tire model was a popular method in the 1960's and 1970's before the empirical approaches became dominating. The brush model gives an educational interpretation of the physics behind the tire behavior and explains that a part of the tire surface in the contact patch to the ground slides on the road surface. Information about the friction coefficient is revealed in the tire behavior even when low tire forces are transmitted. If the the brush model is sufficiently good it is possible to estimate the friction coefficient.

In the thesis the influence of velocity-dependent friction and asymmetric pressure-distribution on the brush model are examined. The latter is used to introduce a calibration factor to improve the agreement of the model to real data. Performed vehicle tests show that sufficient accuracy might be obtained.

The coupling between the longitudinal and lateral tire forces is discussed in detail and a new proposal to derive the combined slip forces from pure slip models is presented. This method relies on the physics from the brush model and includes a velocity dependency which is derived from the pure slip models. All information is extracted automaticly from the models, which allows continuous changes of the tire characteristics. The method shows good agreement to real data.

Key words
Tire model, friction, combined slip, brush model, vehicle

Classification system and/or index terms (if any)

Supplementary bibliographical information

Tire Models for Use in Braking Applications

Jacob Svendenius

Contents

Contents

Acknowledgments

This thesis would not exist without a decision from the technical manager, Kent Jörgensen and the former personal manager, Lena-Maria Lundberg at Haldex Brake Products, giving me the funding to perform this research. I am very grateful for this decision and the opportunity that Haldex has given me. I will also thank my supervisor, Björn Wittenmark, at the Department of Automatic Control for the administrative work he did to establish this cooperative work. His advice, encouraging support and guiding has all the time lead the project in a rewarding direction. A lot of thanks to my supervisor at Haldex, Per-Axel Roth, for always listening and giving good parallels to earlier experiences. My new group of colleagues at Haldex have been a great asset to me and I really appreciate their support in all matters from critical reviewing to practical help in getting data and test results. I am gifted with fantastic coworkers at two different workplaces. The people at the department are very talented and a great source of inspiration. Special thanks to Ph.D. Magnus Gäfvert for the enriching discussions during our work together, I hope it can proceed. It has everyday been a pleasure to have lunch at Sparta with "Spartagänget" and a delight to quarrel with the always benevolent and helpful secretaries and computer staff.

I am really grateful for the encouragement and support from my mother, father and sister. It is good to know that they always care. Thanks to all my friends, many of them have somehow helped me to come to this point.

Finally, I will thank my soon-becoming wife, Malin for her endless love and patience in lost week-ends due to thesis writing. I love you!

Jacob

1

Introduction

1.1 Background and Motivation

Compared to the age of the wheel, the rubber tire is a very recent invention. It started in 1839 when Charles Goodyear discovered the rubber vulcanization process [Continental, 2003]. Solid rubber rings then came to be used around the wheels to reduce the vibration problem and to improve the traction properties. A couple of years later, 1845, Robert W. Thomson patented the air filled tire, but due to its lower durability the idea fell into disuse [Thomson, 2003]. In 1888 John Boyd Dunlope reinvented the pneumatic tire claiming of no knowledge about the prior patent. The patent was mainly directed for bicycles, but soon the advantages of using the pneumatic tires even for cars were discovered and a few years later use of air filled tires was an obligation for driving on the highways. Today, Michelin, which besides Goodyear and Bridgestone, is the largest tire manufacture with approximately 20% of the world market, employs 126 000 workers [Michelin, 2003]. The main tasks for the tire development are now focused on better environment, handling and, water planing properties.

The performance of the tire is of major concern for the vehicle, since it is in the contact patch between the tire and road the forces to control the vehicle are generated. At critical braking and steering maneuvers, exceeding the limits of the tire grip can lead to complete loss of steerability. Therefore, knowledge about the contact properties

is a valuable information for today and future vehicle control systems.

1.2 Outline

The aim with the thesis is to gather information and gain understanding about the behavior of pneumatic tires. The behavior is expressed in mathematical terms. As in many other modeling issues a main question is how to do the simplifications. The tire has a very complex structure and we are trying to obtain the describing formulas as simple as possible. A future goal is to use the results for braking applications and development of stability control strategies.

The introduction is followed by a section explaining the basic concepts used in the thesis. The mechanic and dynamic properties of a tire are briefly discussed and the notation, important for futher reading is introduced. Chapter 3 presents several ways to express the force-slip relation and two different approaches to explain this behavior physically are discussed. The last part of the chapter describes methods to derive the tire characteristics for cases of simultaneous braking and cornering using tire data from pure slip measurements. A new method based on physical modeling is presented. Factors that affects the tire modeling are discussed in Chapter 4. Here also methods to make the brush tire model more accurate and flexible by use of a calibration factors are presented. The final chapter discusses the validity of the brush model and compares it to measurements performed on a real vehicle.

1.3 Contributions and Related Publications

The thesis is based on research presented in three different papers:

Svendenius, J. (2003): "Brush tire model with increased flexibility." European Union Control Association, Cambridge, UK.

Gäfvert, M. and J. Svendenius (2003): "A novel semi-empirical tire model for combined slip." Journal paper, submitted to Vehicle system dynamics.

Svendenius, J. and M. Gäfvert (2003): "A brush-model based semi-empirical tiremodel for combined slips." Conference paper, submitted to the SAE world conference 2004, Detroit.Xb

The research is further explained in the following internal reports:

Gäfvert, M. and J. Svendenius (2003): "Construction of semi empirical tire models for combined slip." Technical Report ISRN LUTFD2/TFRT—7606–SE. Department of Automatic Control, LTH, Sweden.

Svendenius, J. (2003): "Wheel model review and friction estimation." Technical Report ISRN LUTFD2/TFRT—7607–SE. Department of Automatic Control, LTH, Sweden.

2

Pneumatic Tires – Basics

2.1 Tire Mechanics

Design

The pneumatic tire is a flexible structure that together with the rim can hold the pressure of compressed air. Its most important features are to reduce vibrations from unevennesses in the road and to achieve a high friction coefficient to the road surface. The main structural component is the carcass, consisting of layers of stiff cords, which hold the shape of the tire and the tension from the inflated air. High tensile steel wires, called beads, connect the carcass to the rim and when a load is applied on the wheel, the rim primarily hangs on the sidewall cords and the beads. The entire structure is covered with a wear resistant rubber compound, often styrene-butadiene, to protect the carcass and to build up high friction to the road. There are mainly two ways to design the carcass, radial-ply or bias-ply. Radial-ply has the sidewall cords oriented radially and the wear surface cords laid tangentially. The bias-ply tires have the layers diagonally positioned over the entire tire surface as illustrated by Figure 2.1. For a bias-ply tire in operation the deformation of the cords gives rise to a wiping motion of the rubber tread, which causes higher wear and power dissipation. Therefore, radial tires are mostly used for cars and trucks, even though their manufacturing process is more complex and the expense is about
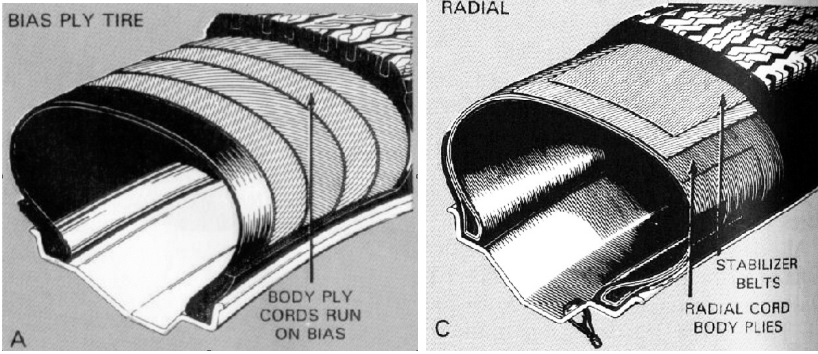
Figure 2.1 Schematic illustration of the difference between bias-ply and radial-ply tire construction. Reprint from [NWT-Consortium, 2002]

50% higher than for a bias-ply tire [Thomson, 2003].

Kinematics

This section describes the relevant tire kinematics and introduces definitions which are used in the following. The entities are illustrated in Figure 2.2. Vectors have two components and are denoted by a bar as in $\bar{v}$. The corresponding components and magnitude are denoted by v_x, v_y, and v. The *wheel-travel velocity* $\bar{v} = (v_x, v_y)$ deviates from the wheel heading by the slip angle α

$$\tan(\alpha) = \frac{v_y}{v_x} \tag{2.1}$$

The circumferential velocity of the wheel is

$$v_c = \Omega R_e \tag{2.2}$$

where Ω is the wheel angular velocity, and R_e the effective rolling-radius of the tire, defined as the ratio v_x/Ω when no longitudinal force is generated by the tire. The *slip velocity*, or the relative motion of the tire in the contact patch to ground, that arises when a horizontal force is transmitted, is

$$\bar{v}_s = (v_x - v_c, v_y) \tag{2.3}$$

12
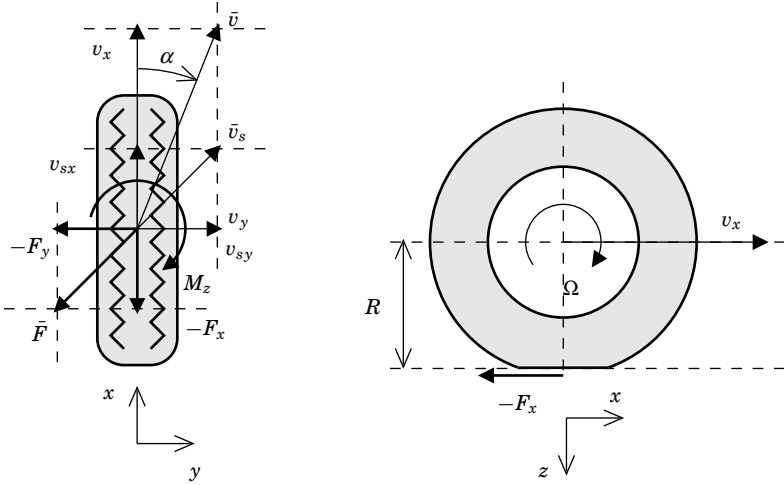
Figure 2.2 Kinematics of an isotropic tire during braking and cornering. Force vectors are also included. (Left: top view; Right: side view)

The direction of the slip velocity is denoted by β where

$$\tan(\beta) = \frac{v_{sy}}{v_{sx}} \qquad (2.4)$$

The *tire slip* is defined by normalizing the slip-velocity with a reference velocity. Three slip definitions are commonly used

$$\bar{\sigma} = \frac{\bar{v}_s}{v_c} \qquad \bar{\kappa} = \frac{\bar{v}_s}{v_x} \qquad \bar{s} = \frac{\bar{v}_s}{v} \qquad (2.5)$$

Note that the slips are collinear with the slip velocity $\bar{v}_s$. It is the custom to describe tire-forces as functions of the slip rather than the slip velocity. This convention is followed also in this work. Implicitly, this assumes that the forces do not depend on the magnitude of the slip velocity, v_s. In general, at least the sliding friction is velocity dependent. There are several conventions on how to define the tire slips, e.g. the ISO and SAE standards [ISO 8855, 1991; SAE Recommended Practice J670e, 1976] use $-100\kappa_x$ [%] to represent longitudinal slip, and α [deg]

for lateral slip. In this report the slips are defined such that signs are consistent for the different slip definitions, and such that a generated tire force has opposite sign to the slip. This means that braking or left cornering will result in positive slip and negative force. For convenience the *slip ratio*, λ, will be used to denote longitudinal slip as: $\lambda = \kappa_x$. It is straightforward to translate between the different slip representations

$$\bar{\sigma} = (\lambda, \tan(\alpha))/(1 - \lambda) = \frac{\bar{\kappa}}{1 - \kappa_x} = \frac{\bar{s}}{\sqrt{1 - s_y^2} - s_x} \tag{2.6a}$$

$$\bar{\kappa} = (\lambda, \tan(\alpha)) = \frac{\bar{\sigma}}{1 + \sigma_x} = \frac{\bar{s}}{\sqrt{1 - s_y^2}} \tag{2.6b}$$

$$\bar{s} = (\lambda \cos(\alpha), \sin(\alpha)) = \frac{\bar{\sigma}}{\sqrt{(1 + \sigma_x)^2 + \sigma_y^2}} = \frac{\bar{\kappa}}{\sqrt{1 + \kappa_y^2}} \tag{2.6c}$$

Forces and Torques

The choice of reference system in this work largely follows the SAE standard [SAE Recommended Practice J670e, 1976], with the longitudinal x-axis aligned with the wheel heading, the lateral y-axis perpendicular to the wheel, and the vertical z-axis pointing downwards, as of Figure 2.3.

The forces of interest for vehicle handling or friction estimation purposes are the planar lateral and longitudinal forces, F_x and F_y, and the self-aligning moment M_z. The longitudinal tire force F_x is generated when braking or driving[1], and the lateral force F_y and the torque M_z when cornering. The self-aligning moment results from the fact that the planar forces have a point of action which is not positioned exactly under the wheel center. The rolling-resistance and overturning moment are not of primary interest in this context and the latter will not be regarded in the following. Likewise, it will be assumed that the camber angle γ is zero. For heavy vehicles this is normally a reasonable approximation.

---

[1]In the following, when the word "braking" is used in the context of longitudinal tire force generation, this will actually mean "braking or driving" unless stated otherwise.
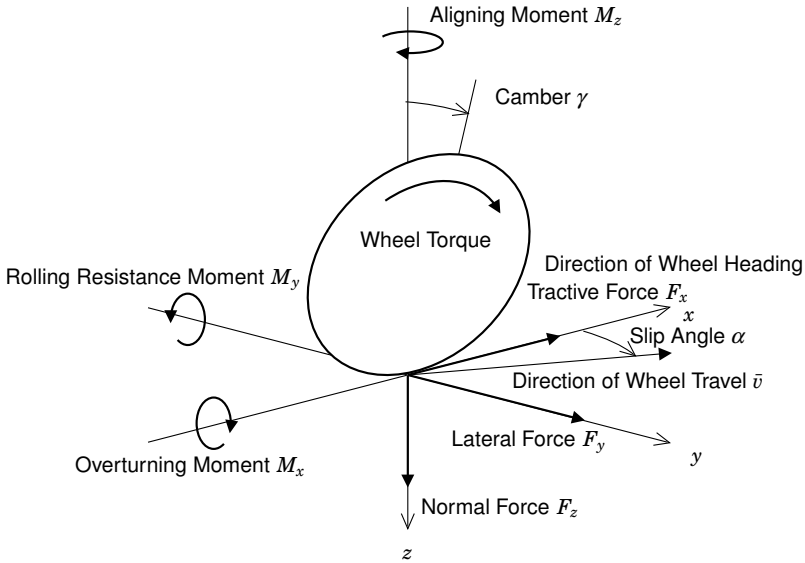
Figure 2.3   Forces and moments acting on a tire [SAE Recommended Practice J670e, 1976].

Relation Between Force and Slip

Pure slip   It is a well known fact that there exits a relation between the horizontal tire force and the slip. The velocity difference between the carcass and the road is a result from continuous deformation of the rubber treads and sliding between the tire and the road surfaces. At low slip the relation is nearly linear and the forces can be described as $F_x = -C_\lambda \lambda$, longitudinally and $F_y = -C_\alpha \alpha$, laterally. The *braking stiffness*, C_λ and the *cornering stiffness*, C_α are correspondingly defined as the linearization of the force-slip relation at $\lambda = 0$ and $\alpha = 0$ [Wong,

2001]

$$C_\lambda = -\left.\frac{dF_x}{d\lambda}\right|_{\lambda=0,\alpha=0} \tag{2.7a}$$

$$C_\alpha = -\left.\frac{dF_y}{d\alpha}\right|_{\lambda=0,\alpha=0} \tag{2.7b}$$

For higher slip the relation is strongly nonlinear and other functions to express the relation are necessary. The normal behavior for a tire on asphalt is that the force increases for increasing slip up to $\lambda^* \approx 0.15$ and then diminishes slightly when λ reaches unity.

Combined slip   Combined slip signifies simultaneous braking and cornering. A steering maneuver during braking generally decreases both the braking stiffness, the longitudinal peak force and its corresponding slip value. Knowledge about the interaction between the slip in both directions is therefore inevitable for more advanced vehicle simulation. In Section 3.3 and 3.4 this topic will be discussed in detail.

Tire Deformation

To reduce the vibrations from unevennesses in the road is one of the main tasks for the tire. Its elastic properties and the ability to deform is therefore of great importance. The tire has to allow large vertical shape changes for good damping. This has the price of slower handling and reaction for maneuvers from the driver, since a softer tire also allows larger horizontal deformation. The deformation of the tire can schematicly be divided between the carcass and the tread. The carcass flexibility is the major source for the dynamics and the rolling resistance and the minor deflection in the rubber treads decides the force-slip characteristics.[2] The stretched string carcass model originates from the work of von Schlippe in 1941 [Pacejka, 2002] and is still used for tire modeling, see for instance [Thorvald, 1998]. The carcass is then, as the name intends, approximated as a stretched string attached to the rim by visco-elastic springs. The method is illustrated in Figure 2.4. Finite element methods are usually used to derive more

---

[2]This holds only in the longitudinal direction. In the lateral case the carcass flexibility will affect the force-slip characteristics, which is discussed in Section 4.4

accurate results for the tire deformation [Pauwelussen *et al.*, 1999], since the shape is complex and the deflections are large and probably outside the linear region. The reason for using the stretched string method is that it results in sufficiently accurate and fairly simple expressions that easily can be used for estimation and control issues and gives a good understanding for the underlying physics.
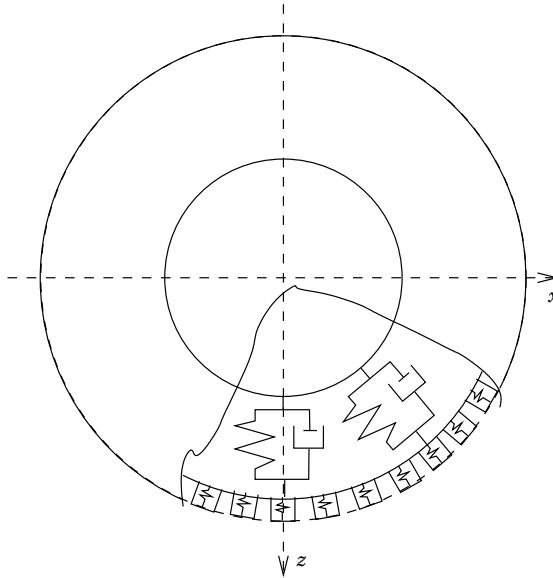
Figure 2.4 Illustration of the schematic tire structure used in this thesis. The carcass is visualized as a stiff string attached to the rim by visco-elastic springs. The springs are only showed in the radial direction but work even tangentially and laterally (out of the wheel plane). The same holds for the elastic tread springs.

Rolling Resistance

The vertical deformation of a tire is often clearly visible. When the vehicle rolls the wheel rotation continuously changes this deformation. Due to the visco-elastic properties of the carcass springs power will dissipate from the system. The effect is called rolling resistance and

is, in general, assumed to depend linearly on the tire load [Wong, 2001]. Hence,

$$M_r = q_0 R F_z \qquad (2.8)$$

For more accurate result the dependency on the velocity has to be included in the tire specific factor, q_0. In the SWIFT tire-model [Pacejka, 2002], this dependence is described as $q_0 = q_1 + q_3 v_x/v_0 + q_4(v_x/v_0)^4$, while in [Wong, 2001] $q_0 = q_1 + q_3 v_x{}^2$ is used. In the latter book also the effect of other factors on the rolling resistance is discussed.

2.2 Tire Dynamics

The effect of the tire dynamics is generally small compared to the effect of the dynamics of the complete vehicle. However, knowledge about the dynamic behavior has become more important in the recent years, since the research and development of fast vehicle control systems has increased extensively. In this kind of system, generally, the forces and movements in the contact patch are of interest. The placement of the sensors limits the measurement of those entities to be performed on the hub. For this reason the behavior of the force transmission between the contact patch and the rim is essential to know.

Longitudinal dynamics The longitudinal dynamics of a tire, due to the deformation can be studied by regarding a lumped version of the stretched string model. The tire walls are approximated as a torsion spring attached to the rim in one end and to the tire belt in the other. The carcass is assumed to be stiff. In Figure 2.5 the mechanical system is illustrated. The torque working on the carcass spring is

$$M_f = C_{cx}(\varphi_c - \varphi_r) + D_{cx}(\dot{\varphi}_c - \dot{\varphi}_r) \qquad (2.9)$$

where C_{cx} is the carcass stiffness and D_{cx} the damping coefficient. Introducing $\Delta\varphi = \varphi_c - \varphi_r$, the following linear system can be established

$$
\begin{bmatrix} \ddot{\varphi}_r \\ \ddot{\varphi}_c \\ \Delta\dot{\varphi} \end{bmatrix} = \begin{bmatrix} \frac{-D_{cx}}{J_r} & \frac{D_{cx}}{J_r} & \frac{C_{cx}}{J_r} \\ \frac{D_{cx}}{J_c} & \frac{-D_{cx}}{J_c} & -\frac{C_{cx}}{J_c} \\ -1 & 1 & 0 \end{bmatrix} \begin{bmatrix} \dot{\varphi}_r \\ \dot{\varphi}_c \\ \Delta\varphi \end{bmatrix} + \begin{bmatrix} 1 & 0 \\ 0 & R \\ 0 & 0 \end{bmatrix} \begin{bmatrix} M_B \\ F_x \end{bmatrix}
$$

$$(2.10)$$
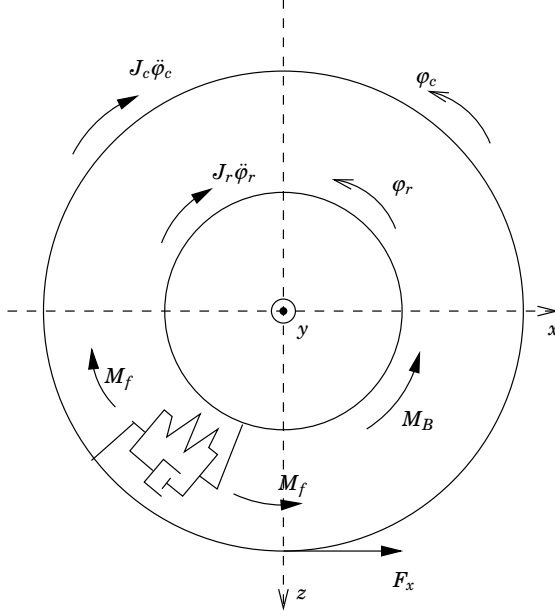
Figure 2.5 Illustration of the torque equilibrium on a tire.

$$y = \begin{bmatrix} 1 & 0 & 0 \end{bmatrix} \begin{bmatrix} \dot{\varphi}_r & \dot{\varphi}_c & \Delta\varphi \end{bmatrix}^T \qquad (2.11)$$

Since almost all vehicles are equipped with wheel speed sensors to measure the rim rotation velocity, it is natural to choose $\dot{\varphi}_r$ as output signal. As mentioned above the deformation of the tire belt and the longitudinal movement of the rim relative the belt are not included in the equations above. This is a restriction since the effects are not neglectable, but will result in the same type of equation structure as the system above with different parameters. The effects can then be included by changes in the parameter matrix.

In many cases the realization above is too detailed and the effect of

the damping and inertia might be neglected. Then tire dynamics will be described by a first order function, with a speed-dependent time-constant, which is a common and accepted method [Pacejka, 2002]. The time constant can be expressed as the time it takes for the wheel to roll a specific distance, σ_c, i.e $T = \sigma_c/v_r$. This entity is often referred to as the relaxation length. The relaxation length can be derived from (2.10), by using the linear relationship between the brake force and the slip $F_x = -C_\lambda \lambda_c = -C_\lambda(1 + R\dot{\varphi}_c/v_x)$. Then regarding $\dot{\varphi}_r$ as the input signal and elimination of the first row, (2.10) becomes

$$
\begin{bmatrix} J_c\ddot{\varphi}_c \\ \Delta\dot{\varphi} \end{bmatrix} = \begin{bmatrix} -D_{cx} + \frac{RC_\lambda}{v_x} & -C_{cx} \\ 1 & 0 \end{bmatrix} \begin{bmatrix} \dot{\varphi}_c \\ \Delta\varphi \end{bmatrix} + \begin{bmatrix} D_{cx} \\ -1 \end{bmatrix} \dot{\varphi}_r - \begin{bmatrix} RC_\lambda \\ 0 \end{bmatrix}
\tag{2.12}
$$

Putting J_c, D_{cx} to zero gives

$$
\dot{\varphi}_c \frac{RC_\lambda}{v_x} = RC_\lambda - C_{cx}(\varphi_c - \varphi_r)
\tag{2.13}
$$

Time differentiation, laplace transform and exchange of φ to λ, the expression can be rewritten as

$$
\lambda_c = \frac{1}{\dfrac{R^2 C_\lambda}{v_x C_{cx}} s + 1} \lambda_r
\tag{2.14}
$$

which gives $\sigma_c = R^2 C_\lambda/C_{cx}$. Note that this approximation only holds for slip changes at low slip, where the linear approximation for the force slip behavior still holds and $v_x = v_r$. For large torque variations at higher slip, i.e. in an ABS-braking situation (2.10) is preferred.

In the lateral direction the relaxation-length concept for low slip is experimentally proved as well [Pacejka, 2002]. However, a more detailed analysis is difficult to perform, since the string approach allows the carcass to have a variable lateral deformation tangentially. For steady state conditions this is further discuss in Section 4.4, but for the dynamic case the discussion is left outside the scope of this thesis.

3

Modeling Tires

Much research has been done in the area of modeling tires and it covers all from simple models aiming at understanding the physics to advanced finite-element models that precisely can predict the behavior. The tire modeling was initiated by the vehicle and air craft industry back in the 1940's. The researchers first described the tire characteristics from physical modeling. Later on the complex nature of the tire increased the interest for finding equation structures that easily could be adjusted to fit the measurements from the tire tests. The traditional tire models only covered the static force-slip relation, but the development of fast control system has now increased the focus on the dynamical aspects of the tire behavior.

3.1 Tire Characteristic Functions

The aim of the force-slip describing functions is to supply a structure that can fit measurement data well by optimal choice of included parameters. The first tire models were derived from variants of the brush model, see Section 3.2, and often resulted in a third order polynomial including two parameters. One example is the proposal for the lateral force by Smiley and Horne (1958) described in [Nguyen and Case, 1975]

$$F_{0y} = \begin{cases} C_\alpha \alpha \left(1 - \dfrac{\alpha^2}{3(\alpha^\circ)^2} \right) & \alpha \leq \alpha^\circ = \dfrac{3\mu F_z}{2C_\alpha} \\ \mu F_z & \text{otherwise} \end{cases} \qquad (3.1)$$

where C_α is the cornering stiffness and μ the friction coefficient. The definition of the slip angle α is given by (2.1). The friction is assumed to be constant in the model, which disables it from characterizing the brake force accurately for large slips. By use of different, physical constraints in the modeling Dugoff derived the relation

$$F_{0y} = \begin{cases} C_\alpha \tan(\alpha) & \alpha \leq \alpha^\circ \\ \mu F_z \left(1 - \dfrac{\mu F_z}{4 C_\alpha \tan \alpha} \right) & \text{otherwise} \end{cases} \tag{3.2}$$

where

$$\alpha^\circ = \arctan(\mu_0 F_z / 2 C_\alpha + \varepsilon v \mu_0 F_z)$$
$$\mu = \mu_0 (1 - \varepsilon v \tan(\alpha))$$
$$\mu_0 : \text{Nominal friction coefficient}$$
$$\varepsilon : \text{tire constant}$$

Here a dependency of the vehicle speed is included to express the behavior of the brake force for large slip. To increase the flexibility further Holmes proposed an empirical structure, quite different to the others, to use for curve fitting

$$F_{0y} = a_0 + a_1 v_x + a_2 v_x^2 + a_3 \alpha + a_4 \alpha^2 + a_5 \alpha^3 + a_6 R + a_7 P \tag{3.3}$$

where P is a tire pattern constant and R is a tire tread constant, but $a_{1...7}$ have no physical interpretation. All the approaches above characterize the relation between the lateral force and the lateral pure-slip, but can with minor changes also be used to express the longitudinal behavior of the tire. In [Kiencke and Nielsen, 2000] a model is used where the input s_{Res} denotes the resultant slip $(s_L^2 + s_S^2)^{1/2}$ and even one slip definition (compare to Equation (2.5)) is used in $s_L = (v_c \cos(\alpha) - v_x)/v_x$ and $s_S = v_c \sin(\alpha)/v_x$ perpendicular to each other. The model can then be used for combined slip situations and the direction of the resulting force is collinear to the slip vector $\bar{s}_{\text{Res}}$. To complicate it even further the direction of s_L is the direction of the wheel travel, $\bar{v}$ in distinction to the slip direction used in this thesis, v_x which corresponds to the

wheel plane. Also nonlinear effects of the wheel load can be accounted for in this model, which originally was developed by Burckhardt

$$F = (a_1 (1 - \exp(-a_2 s_{\text{Res}})) - a_3 s_{\text{Res}}) \, e^{-c_4 s_{\text{Res}} v} (1 - c_5 F_z^2) \qquad (3.4)$$

A disadvantage in the approach is that the tire characteristic is assumed to be equal in both the lateral and the longitudinal direction. Due to the influence of the carcass flexibility, which is further discussed in Section 4.4, this is generally not the case. A way to describe the lateral force and account for combined braking and cornering, without the assumption on isotropicity, has been proposed by Chiesa.

$$F_y = \sqrt{1 - \left(\frac{F_x}{2\mu N} \right)^n} F_z \left((a_1 + a_2 F_z)\alpha + (a_3 + a_4 F_z)\alpha^2 + \dots \right) \quad (3.5)$$

The method requires that the longitudinal force is known which not is obvious. In 1987 H.B. Pacejka presented the "Magic Formula", which now has become the predominating model [Bakker *et al.*, 1987]. The model expresses the lateral and longitudinal tire forces, as well as aligning torque, on the form

$$y(x) = D \sin(C \arctan((1 - E)x + (E/B) \arctan(Bx))) \qquad (3.6)$$

where (x, y) is (λ, F_{0x}), (α, F_{0y}), or (α, M_{0z}). The four coefficients have interpretations as stiffness factor (B), shape factor (C), peak factor (D), and curvature factor (E), and are unique for each of F_x, F_y, and M_z. Approximation of the normal load dependence may be introduced as $D = a_1 F_z^2 + a_2 F_z$, $BCD = (a_3 F_z^2 + a_4 F_z)/e^{a_5 F_z}$, and $E = a_6 F_z^2 + a_7 F_z + a_8$. The Magic Formula has been improved to adjust for combined slip. The pure slip forces are then multiplied by factors that are dependent on the slips (λ, α). These factors include additional parameters that require further data to be estimated. The self-aligning torque is derived by scaling of M_{0z} and an addition of scaled pure-slip forces. This is a part in the SWIFT-model [Pacejka, 2002], which is large set of equations describing most aspects of the tire behavior and its dependence on related factors. An extensive amount of measurement data is necessary for this description.

A number of different equations to describe the tire behavior has been reviewed in this section. It is impossible to give a complete view of the results presented and published in this area, but a more detailed description can be found in [Nguyen and Case, 1975]. The important point is, however, to show on the variety and width of the expressions and approaches that have proposed in the literature.

3.2 Physical Tire Models

The Brush Model

The brush model is a well-known approach to model tire forces, see e.g. [Pacejka, 1988], [Pacejka, 2002] or [Wong, 2001]. The model was very popular in the 1960's and 1970's before the empirical approaches became dominating and it describes the physics behind the tire behavior in an educational way. In this section the brush-model concept is applied to combined slips, much like the approach of [Gim and Nikravesh, 1991]. The brush model describes the generation of tire forces based on partitioning of the contact patch into an adhesion and a slide region. Forces in the adhesive region are assumed to be caused by elastic deformation in the rubber volume that is between the tire carcass and the ground. The carcass is assumed to be stiff, which means that effects of carcass deformation are neglected. In the sliding region forces are caused by sliding friction.

The model is obtained by dividing the rubber volume in the contact region into small brush elements. Each element stretches laterally over the entire contact region, but their length is infinitesimal in the longitudinal direction. The elements are regarded as elastic rectangular blades, or bristles, see Figure 3.1. Even though rubber in general is not linearly elastic, this assumption is made in the brush model. Positions in the contact region are expressed in a reference system attached to the carcass, with the origin located in the center of the contact region. The length of the contact region is $2a$. Each bristle is assumed to deform independently in the longitudinal and lateral directions. In the adhesive region the bristles adhere to the road surface and the deformation force is carried by static friction. In the sliding
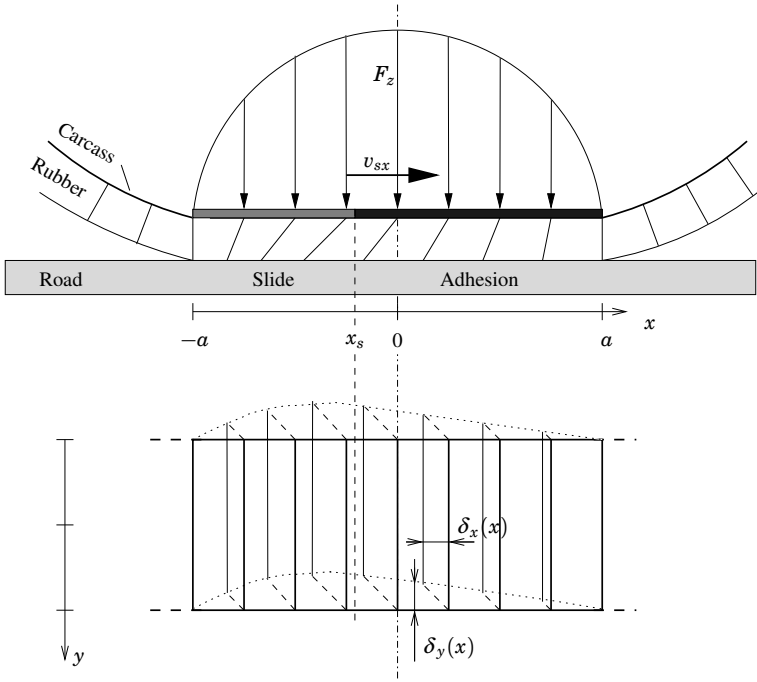
Figure 3.1 The deformation of the rubber layer between the tire carcass and the road according to the brush model. The carcass moves with the velocity v_{sx} relative the road. The contact zone moves with the vehicle velocity v_x. (Top: side view; Bottom: top view)

region the bristles slide on the road surface under influence of sliding friction. Hence, in the sliding region the resulting force is independent of the bristle deformations.

Adhesive bristle forces Regard the specific infinitesimal bristle which is attached to the carcass at position x relative the origo in the center of the contact patch. Assume that this bristle belongs to the adhesive region. The bristle is in contact with the road surface at position $x_r(x)$, $y_r(x)$, see Figure 3.2. Since there is no sliding in the

adhesive region the contact-point position may be described by

$$x_r(x) = a - \int_0^{t_c(x)} v_x \, dt \qquad (3.7a)$$

$$y_r(x) = - \int_0^{t_c(x)} v_y \, dt \qquad (3.7b)$$

where $t_c(x)$ is the time elapsed since the bristle entered the contact region. The velocities v_c, v_x and v_y are assumed to be constant as a bristle travels through the adhesive region of the contact patch, i.e., during the integration interval $[0, t_c(x)]$. Hence, the bristle position is $x = a - v_c t_c(x)$, and $t_c(x) = (a - x)/v_c$. The deformation of the bristle is

$$\delta_x(x) = x_r(x) - x \qquad (3.8a)$$
$$\delta_y(x) = y_r(x) \qquad (3.8b)$$

Insertion of (3.7) and the expression for $t_c(x)$ yields

$$\delta_x(x) = -\frac{v_x - v_c}{v_c}(a - x) = -\sigma_x(a - x) \qquad (3.9a)$$

$$\delta_y(x) = -\frac{v_y}{v_c}(a - x) = -\sigma_y(a - x) \qquad (3.9b)$$

where the slip definition from (2.5) is used in the last equality. With the assumption of linear elasticity, the deformation force corresponding to (3.8) is

$$dF_{ax}(x) = c_{px} \, dx \, \delta_x(x) \qquad (3.10a)$$
$$dF_{ay}(x) = c_{py} \, dx \, \delta_y(x) \qquad (3.10b)$$

where c_{px} and c_{py} are the longitudinal and lateral bristle stiffnesses per unit length. The assumption of constant v_c, v_x, v_y in the interval $[0, t_c(x)]$ is relaxed to the assumption of slow variations in σ_x and σ_y with respect to the duration $2a/v_c$, which is the maximum time for a bristle to travel through the adhesion region. The total adhesive tire
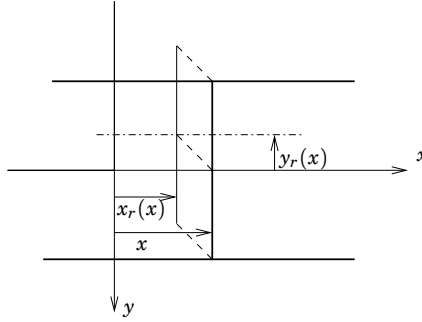
Figure 3.2 The deformation of a bristle element in the contact patch. Compare with Figure 3.1.

force is computed by integration of (3.10) over the adhesive region. With (3.9) this gives

$$F_{ax} = \int_{x_s}^{a} dF_{ax}(x) = -c_{px}\sigma_x \int_{x_s}^{a} (a - x) \, dx \qquad (3.11a)$$

$$F_{ay} = \int_{x_s}^{a} dF_{ay}(x) = -c_{py}\sigma_y \int_{x_s}^{a} (a - x) \, dx \qquad (3.11b)$$

where x_s is the position in the contact patch which divides the adhesive and sliding regions. To compute total adhesive force it is necessary to know x_s.

The size of the adhesion region   The size of the adhesive region is determined by the available static friction. The deformation will be limited by the largest force that can be carried by the static friction between the tire and the road. The static friction is assumed to be anisotropic with the friction coefficients μ_{sx} and μ_{sy}, respectively. With a normal force $dF_z(x)$ acting on the infinitesimal bristle at position x, the available static friction force is described by the elliptic constraint

$$\left(\frac{dF_{ax}(x)}{dF_z(x)\mu_{sx}} \right)^2 + \left(\frac{dF_{ay}(x)}{dF_z(x)\mu_{sy}} \right)^2 \leq 1 \qquad (3.12)$$
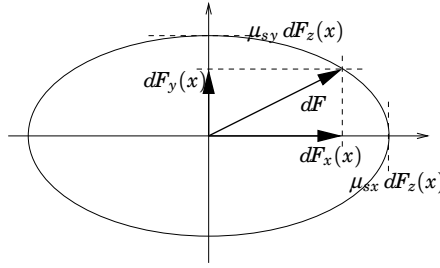
Figure 3.3 Illustration of the elliptic static friction constraint at anisotropic friction and rubber characteristics. Note that the direction of $d\bar{F}(x)$ and $\bar{\sigma}$ is equal only if $c_{px}/c_{py} = \mu_{sx}/\mu_{sy}$.

As a result, the magnitude of the available static friction force is dependent of the direction of the deformation force $d\bar{F}_a(x)$, defined by (3.10). The static friction constraint is illustrated in Figure 3.3. When $d\bar{F}_a(x)$ exceeds the static friction constraint the bristle will leave the adhesive region and start to slide. Introduce the pressure distribution $q_z(x)$, with $dF_z(x) = q_z(x)\,dx$. By combining (3.9) and (3.10) with (3.12) the static friction constraint may be written as

$$\sqrt{\left(\frac{c_{px}\sigma_x}{\mu_{sx}}\right)^2 + \left(\frac{c_{py}\sigma_y}{\mu_{sy}}\right)^2}\,(a - x) \leq q_z(x) \tag{3.13}$$

The position x_s in the contact area is the break-away point where the static friction limit is reached and the bristles starts to slide. If the pressure distribution $q_z(x)$ is known then x_s can be calculated by setting equality in (3.13) with $x = x_s$.

A common assumption is to describe the pressure distribution in the contact patch as a parabolic function:

$$q_z(x) = \frac{3F_z}{4a}\left(1 - \left(\frac{x}{a}\right)^2\right) \tag{3.14}$$

This is proposed, for example, in [Pacejka, 1988] and has shown to give a good agreement with experimental longitudinal force-slip curves for

real tires. In Section 4.1 the influence of the pressure distribution is further examined. Inserting (3.14) in (3.13) with equality gives

$$\sqrt{\left(\frac{c_{px}\sigma_x}{\mu_{sx}}\right)^2 + \left(\frac{c_{py}\sigma_y}{\mu_{sy}}\right)^2}\,(a - x_s) = \frac{3F_z}{4a^3}\,(a - x_s)\,(a + x_s) \qquad (3.15)$$

The solution for the break-away point x_s is then

$$x_s(\sigma_x, \sigma_y) = \frac{4a^3}{3F_z}\sqrt{\left(\frac{c_{px}\sigma_x}{\mu_{sx}}\right)^2 + \left(\frac{c_{py}\sigma_y}{\mu_{sy}}\right)^2} - a \qquad (3.16)$$

Since x_s is a point in the contact patch it must belong to the interval $[-a, a]$. If $x_s = a$ the entire contact patch is sliding. In the case of pure slip, i.e. either σ_x or σ_y is zero, this will occur at the slips $\sigma_x = \sigma_x^\circ$ or $\sigma_y = \sigma_y^\circ$ with σ_x° and σ_y° given by the following definition.

DEFINITION 3.1—LIMIT SLIPS
Define the limit slips as

$$\sigma_x^\circ \triangleq \frac{3F_z\mu_{sx}}{2a^2 c_{px}} \qquad (3.17a)$$

$$\sigma_y^\circ \triangleq \frac{3F_z\mu_{sy}}{2a^2 c_{py}} \qquad (3.17b)$$

$\square$

Introduction of normalized slips with respect to the limit slips will simplify the notation in the following.

DEFINITION 3.2—NORMALIZED SLIP
Define the normalized slip as

$$\psi(\sigma_x, \sigma_y) \triangleq \sqrt{\left(\frac{\sigma_x}{\sigma_x^\circ}\right)^2 + \left(\frac{\sigma_y}{\sigma_y^\circ}\right)^2} \qquad (3.18)$$

$\square$

Equation (3.16) may now be rewritten as

$$x_s(\sigma_x, \sigma_y) = (2\psi(\sigma_x, \sigma_y) - 1)a \tag{3.19}$$

It is clear that partial sliding occurs when $\psi(\sigma_x, \sigma_y) < 1$. At full sliding then $(\psi(\sigma_x, \sigma_y) \geq 1)$ and $F_{ax}(\sigma_x, \sigma_y) = F_{ay}(\sigma_x, \sigma_y) = 0$. In the following the construction of adhesive and sliding forces at partial sliding will be determined.

Total adhesion force   Knowing the size of the adhesive region, $x_s(\sigma_x, \sigma_y)$, given by (3.19), the adhesive forces are obtained by solving the integrals (3.11) yielding:

$$F_{ax}(\sigma_x, \sigma_y) = -2a^2 c_{px}\sigma_x \left(1 - \psi(\sigma_x, \sigma_y)\right)^2 \tag{3.20a}$$

$$F_{ay}(\sigma_x, \sigma_y) = -2a^2 c_{py}\sigma_y \left(1 - \psi(\sigma_x, \sigma_y)\right)^2 \tag{3.20b}$$

for $(\psi(\sigma_x, \sigma_y) < 1)$. At full sliding $(\psi(\sigma_x, \sigma_y) \geq 1)$ the forces equals $F_{ax}(\sigma_x, \sigma_y) = F_{ay}(\sigma_x, \sigma_y) = 0$. Special notations for the forces at pure slip are introduced as

$$F_{0ax}(\sigma_x) \triangleq F_{ax}(\sigma_x, 0) \tag{3.21a}$$

$$F_{0ay}(\sigma_y) \triangleq F_{ay}(0, \sigma_y) \tag{3.21b}$$

Note that it follows from (3.10) and (3.9) that the produced adhesive force per unit length in the adhesion region is not affected by combined slips:

$$\frac{dF_{ax}(\sigma_x, x)}{dx} = -c_{px}\sigma_x (a - x) \tag{3.22a}$$

$$\frac{dF_{ay}(\sigma_y, x)}{dx} = -c_{py}\sigma_y (a - x) \tag{3.22b}$$

The adhesive forces thus grow linearly with slopes $c_{px}\sigma_x$ and $c_{py}\sigma_y$ as the contact element moves into the adhesion region. To illustrate the generation of the adhesive force the case of pure longitudinal slip is regarded, i.e. $\sigma_y = 0$. From (3.13) the size of the contact region is determined by the point where $c_{px}\sigma_x (a - x) = \mu_{sx}q_z(x)$. That is,
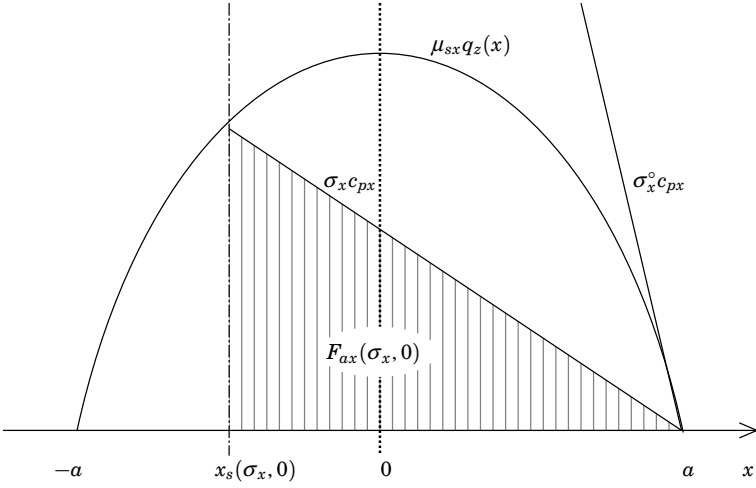
Figure 3.4 Illustration of the adhesive tire-force for pure longitudinal slip. The elastic deformation force for an element at x in the adhesive region depends linearly on x as $c_{px}\sigma_x(x-a)$, where the slope is proportional to the slip σ_x. The transition from adhesion to slide occurs at the cut of the lines at the break-away point x_s. For slips $\sigma_x > \sigma_x^\circ$ full sliding occur in the contact area since there is then no intersection.

where the straight line describing the produced force per unit length cuts $\mu_{sx}q_z(x)$, as is shown in Figure 3.4. The striped area under the line corresponds to the total adhesion force. The slope corresponding to full sliding, i.e. $\sigma_x = \sigma_x^\circ$ is also shown. The case of pure lateral slip is analogous.

Combined-slip slide forces The normal force acting on the sliding region at partial sliding may be computed from (3.14) and (3.19) as

$$F_{sz}(\sigma_x, \sigma_y) = \int_{-a}^{x_s(\sigma_x, \sigma_y)} q_z(x)\,dx = F_z\psi^2(\sigma_x, \sigma_y)\left(3 - 2\psi(\sigma_x, \sigma_y)\right)$$

$$(3.23)$$

In case of isotropic sliding friction with the friction coefficient μ_k, the friction force is collinear with the slip velocity with the magnitude

$F_{sz}(\sigma_x, \sigma_y)\mu_k$ and its components are given by

$$F_{sx}(\sigma_x, \sigma_y) = -\cos(\beta)\mu_k F_{sz}(\sigma_x, \sigma_y) \qquad (3.24a)$$
$$F_{sy}(\sigma_x, \sigma_y) = -\sin(\beta)\mu_k F_{sz}(\sigma_x, \sigma_y) \qquad (3.24b)$$

where β is defined by (2.4). Assumptions on isotropic sliding friction are common in tire modeling, see e.g. [Schuring *et al.*, 1996].

If the sliding-friction is anisotropic with the different friction coefficients μ_{kx} and μ_{ky}, there are several ways to calculate the magnitude and the direction of the resulting force. Three different methods are presented in the following and which one to choose depends on the assumptions made on the friction behavior for the actual case.

Collinear slide forces This method should be used if the friction between two surfaces is supposed to be isotropic, but the values of μ_{kx} and μ_{ky} are unequal. A reason for that could for example be measurement errors. The friction forces given by

$$F_{sx}(\sigma_x, \sigma_y) = -\cos(\beta^-)\mu_{kx} F_{sx}(\sigma_x, \sigma_y) \qquad (3.25a)$$
$$F_{sy}(\sigma_x, \sigma_y) = -\sin(\beta^-)\mu_{ky} F_{sy}(\sigma_x, \sigma_y) \qquad (3.25b)$$

where β^- is defined as

$$\tan(\beta^-) \triangleq \left(\frac{\mu_{ky}}{\mu_{kx}}\right)^{-1} \frac{v_{sy}}{v_{sx}}. \qquad (3.26)$$

which ensures that $\bar{F}_s$ acts in the opposite direction to the sliding motion, with a friction coefficient that is somewhere in the interval $[\mu_{kx}, \mu_{ky}]$ depending on the sliding angle β.

Maximum dissipation rate The correct way to treat anisotropic friction according to the literature is to apply the Maximum Dissipation Rate (MDR) principle. This theory which is further presented in [Goyal, 1989] says that the resulting sliding-friction force $\bar{F}_s''$ is the one which maximizes the mechanical work $W = -\bar{v}_s \cdot \bar{F}_s''$ under the constraint

$$\left(\frac{F_{sx}''}{F_{sz}\mu_{kx}}\right)^2 + \left(\frac{F_{sy}''}{F_{sz}\mu_{ky}}\right)^2 \leq 1. \qquad (3.27)$$

This results in the sliding forces

$$F''_{sx}(\sigma_x, \sigma_y) = -\frac{\mu_{kx}^2 v_{sx}}{\sqrt{(\mu_{kx} v_{sx})^2 + (\mu_{ky} v_{sy})^2}} F_{sz}(\sigma_x, \sigma_y) = -\mu_{kx} \cos{(\beta')} F_{sz}$$
$$(3.28a)$$

$$F''_{sy}(\sigma_x, \sigma_y) = -\frac{\mu_{ky}^2 v_{sy}}{\sqrt{(\mu_{kx} v_{sx})^2 + (\mu_{ky} v_{sy})^2}} F_{sz}(\sigma_x, \sigma_y) = -\mu_{ky} \sin{(\beta')} F_{sz}$$
$$(3.28b)$$

where β' is defined as

$$\tan(\beta') \triangleq \frac{\mu_{ky}}{\mu_{kx}} \frac{v_{sy}}{v_{sx}} \qquad (3.29)$$

The angle of the resulting force $\bar{F}''_s$ is denoted by β'' and is given by

$$\tan(\beta'') = \left(\frac{\mu_{ky}}{\mu_{kx}}\right)^2 \frac{v_{sy}}{v_{sx}} \qquad (3.30)$$

Slip-projection method An intermediate approach to model aniso-tropic sliding friction is to simply replace μ_k in (3.24) with μ_{kx} and μ_{ky} in the corresponding directions:

$$F'_{sx}(\sigma_x, \sigma_y) = -\cos{(\beta)} \mu_{kx} F_{sz}(\sigma_x, \sigma_y) \qquad (3.31a)$$
$$F'_{sy}(\sigma_x, \sigma_y) = -\sin{(\beta)} \mu_{ky} F_{sz}(\sigma_x, \sigma_y) \qquad (3.31b)$$

This means a projection of the pure-slip sliding-forces on the slip vector. The angle of the resulting force is then equal to β'. From the definitions of β (2.4), β' (3.29) and β'' (3.30), it is clear that the direction of $\bar{F}'_s$ will lie between the directions of $\bar{F}_s$ and $\bar{F}''_s$, see Figure 3.5.

To summarize: The sliding forces are described by

$$F_{sx}(\sigma_x, \sigma_y) = -\cos(\beta_{\mathrm{f}}) \mu_{kx} F_{sz}(\sigma_x, \sigma_y) \qquad (3.32a)$$
$$F_{sy}(\sigma_x, \sigma_y) = -\sin(\beta_{\mathrm{f}}) \mu_{ky} F_{sz}(\sigma_x, \sigma_y) \qquad (3.32b)$$
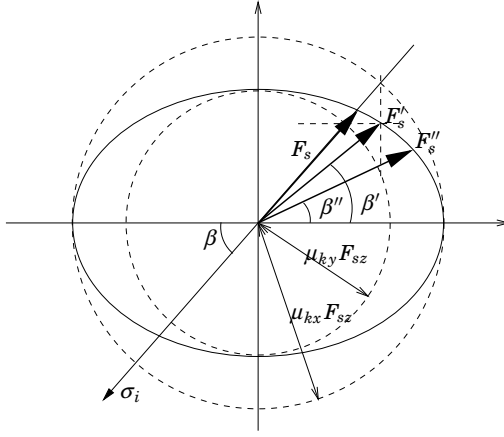
Figure 3.5 Illustration of methods to describe kinetic friction in case of different longitudinal and lateral friction coefficients.

with

$$F_{sz}(\sigma_x, \sigma_y) = F_z \psi^2(\sigma_x, \sigma_y) \left(3 - 2\psi(\sigma_x, \sigma_y)\right) \qquad (3.33)$$

and β_{f} is any of β^- (collinear), β (slip-projection) or β' (MDR) depending on choice of friction model:

$$\tan(\beta^-) \triangleq \left(\frac{\mu_{ky}}{\mu_{kx}}\right)^{-1}\frac{v_{sy}}{v_{sx}} \quad \tan(\beta) \triangleq \left(\frac{v_{sy}}{v_{sx}}\right) \quad \tan(\beta') \triangleq \left(\frac{\mu_{ky}}{\mu_{kx}}\right)\frac{v_{sy}}{v_{sx}} \quad (3.34)$$

In the special case of pure-slip the sliding-forces are

$$F_{0sx}(\sigma_x) = -\mu_{kx}F_{sz}(\sigma_x, 0)\,\mathrm{sgn}(\sigma_x) \qquad (3.35\mathrm{a})$$
$$F_{0sy}(\sigma_y) = -\mu_{ky}F_{sz}(0, \sigma_y)\,\mathrm{sgn}(\sigma_y) \qquad (3.35\mathrm{b})$$

In Figure 3.6 the case of pure longitudinal slip is again regarded, now with also the sliding force introduced. Since $q_z(x)$ is the normal force per unit length, the sliding force per unit length is simply $\mu_{kx}q_z(x)$, as marked in the figure. The horizontally striped area corresponds to the total sliding force.
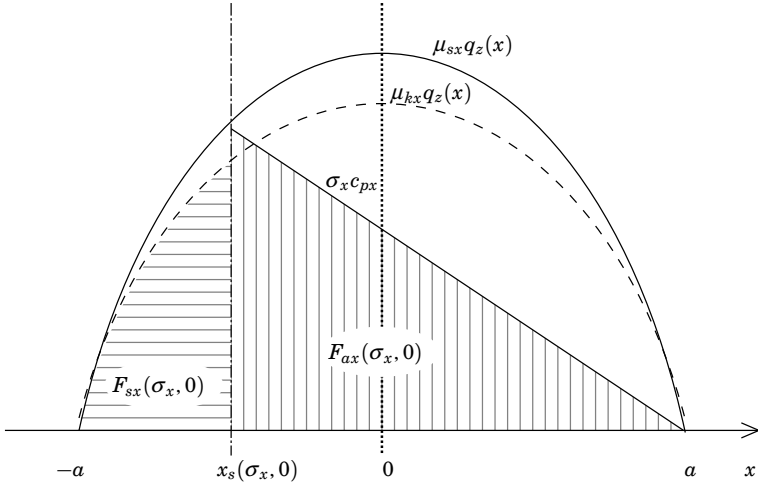
Figure 3.6   Illustration of partition of the contact area into a sliding and an adhesive region for the case of pure longitudinal slip. The slide force for an element at x is determined by the pressure distribution $\mu_{kx}q_z(x)\,dx$. The horizontally striped area is the total slide force.

Effects of combined slips   The total tire force is given by adding the adhesive forces of (3.20) and the sliding forces of (3.32):

$$F_x(\sigma_x, \sigma_y) = F_{ax}(\sigma_x, \sigma_y) + F_{sx}(\sigma_x, \sigma_y) \tag{3.36a}$$

$$F_y(\sigma_x, \sigma_y) = F_{ay}(\sigma_x, \sigma_y) + F_{sy}(\sigma_x, \sigma_y) \tag{3.36b}$$

To illustrate the effect of combined slips Figure 3.7 shows the production of longitudinal force in the case of combined longitudinal and lateral slip (σ_x, σ_y) with $\sigma_x \neq 0$, $\sigma_y \neq 0$. From (3.19) it is clear that the adhering region shrinks compared to the case with pure slip $(\sigma_x, 0)$. The sliding region grows accordingly. From (3.22) it is clear that the adhesive force per unit length is the same for the combined slip (σ_x, σ_y) as for the pure-slip $(\sigma_x, 0)$. Hence, the slope is the same, but the area corresponding to the force is smaller since the adhering region is smaller. The corresponding adhesive-force slope derived from (3.22) is $c_{px}\sigma_x^\circ \psi(\sigma_x, \sigma_y)$. The corresponding expression applies

35
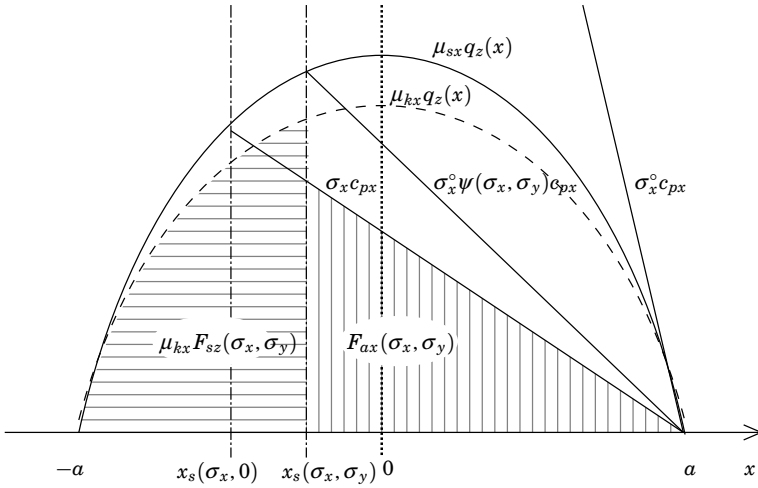
Figure 3.7 Illustration of the effect of combined slip. The combined-slip has the effect of decreasing the size of the adhesive region, compare with Figure 3.6.

for the lateral force. It is therefore clear that sliding will occur simultaneously in both directions as $\psi(\sigma_x, \sigma_y)$ approaches unity. It is important to note that the indicated area under the pressure distribution no longer corresponds to the resulting sliding force. Instead it describes $\mu_{kx} F_{sz}(\sigma_x, \sigma_y)$, which is the force that would result for pure longitudinal sliding with the sliding region $x_s(\sigma_x, \sigma_y)$. This force must be limited by a friction constraint according to Section 3.2.

The braking and cornering stiffnesses are the linearizations of the pure-slip friction curves at small slips and may be computed by derivation of (3.36):

$$C_x = - \left. \frac{\partial F_x(\sigma_x, 0)}{\partial \sigma_x} \right|_{\sigma_x = 0} = 2c_{px}a^2 \tag{3.37a}$$

$$C_y = - \left. \frac{\partial F_y(0, \sigma_y)}{\partial \sigma_y} \right|_{\sigma_y = 0} = 2c_{py}a^2 \tag{3.37b}$$

Self-aligning torque   The self-aligning torque consists of two parts. The main part is M_z', which is the torque developed by the non symmetric distribution of the lateral force F_y. An additional part M_z'' comes up due to the deformation of the tire.

The torque dM_z' developed at position x in the contact region is

$$dM_z'(x) = dF_y(x)\, x \tag{3.38}$$

In the adhesive part of the contact region the expression for $dF_y(x)$ is given by (3.10) together with (3.9). In the sliding zone it is instead given by differentiating (3.32) using $dF_z(x) = q(x)\, dx$. Integration over the adhesive and sliding area separately gives

$$M_{az}'(\sigma_x, \sigma_y) = -c_{py}\sigma_y \int_{x_s(\sigma_x,\sigma_y)}^{a} x\,(a - x)\, dx$$
$$= -c_{py}a^3\sigma_y\frac{2}{3}(1 - \psi(\sigma_x, \sigma_y))^2(4\psi(\sigma_x, \sigma_y) - 1) \tag{3.39}$$

$$M_{sz}'(\sigma_x, \sigma_y) = -\mu_{ky} \sin(\beta) \int_{-a}^{x_s(\sigma_x,\sigma_y)} x\, q_z(x)\, dx$$
$$= -3\mu_{kx} \sin(\beta) a F_z \psi^2(\sigma_x, \sigma_y)(1 - \psi(\sigma_x, \sigma_y))^2 \tag{3.40}$$

$$M_z'(\sigma_x, \sigma_y) = M_{az}'(\sigma_x, \sigma_y) + M_{sz}'(\sigma_x, \sigma_y) \tag{3.41}$$

When there is a lateral slip the tire deflects laterally and the point of action for the longitudinal force will have an offset from the central plane of the wheel. This produces an additional deformation torque in the z-direction. A longitudinal deflection together with a lateral force has the same effect. Since it is assumed that the carcass is stiff the deformation is here described by bristle deflections. The deformation torque developed at position x in the contact region is then described by

$$dM_z''(x) = dF_y(x)\delta_x(x) - dF_x(x)\delta_y(x) \tag{3.42}$$

In the same way as above, integration over the adhesive and the sliding regions is performed separately. The deformation $\delta_x(x)$ is computed

from (3.9) in the adhesive region and from (3.10) using the infinitesimal sliding force in the sliding region. Hence

$$
M_{az}''(\sigma_x, \sigma_y) = \int_{x_s(\sigma_x,\sigma_y)}^{a} c_{py}\sigma_y(a-x)\sigma_x(a-x)\,dx
$$
$$
- \int_{x_s(\sigma_x,\sigma_y)}^{a} c_{px}\sigma_x(a-x)\sigma_y(a-x)\,dx
$$
$$
= \frac{4}{3}(C_y - C_x)a\sigma_x\sigma_y(1 - \psi(\sigma_x,\sigma_y))^3
$$
$$
= \frac{4}{3}\left(\frac{1}{C_x} - \frac{1}{C_y}\right)\frac{a}{(1-\psi(\sigma_x,\sigma_y))}F_{ax}(\sigma_x,\sigma_y)F_{ay}(\sigma_x,\sigma_y) \quad (3.43)
$$

$$
M_{sz}''(\sigma_x, \sigma_y) = \int_{-a}^{x_s(\sigma_x,\sigma_y)} \mu_{ky}\sin(\beta_f)q_z(x)\mu_{kx}^2\cos(\beta_f)\frac{1}{c_{px}}q_z(x)\,dx
$$
$$
- \int_{-a}^{x_s(\sigma_x,\sigma_y)} \mu_{kx}\cos(\beta_f)q_z(x)\mu_{ky}\sin(\beta_f)\frac{1}{c_{py}}q_z(x)\,dx
$$
$$
= \frac{6}{5}\left(\frac{1}{C_x} - \frac{1}{C_y}\right)\mu_{kx}\mu_{ky}a\sin(\beta_f)\cos(\beta_f)F_z^2
$$
$$
\cdot\,\psi^3(\sigma_x,\sigma_y)(10 - 15\psi(\sigma_x,\sigma_y) + 6\psi^2(\sigma_x,\sigma_y))
$$
$$
= \frac{6}{5}\left(\frac{1}{C_x} - \frac{1}{C_y}\right)\frac{a(10 - 15\psi(\sigma_x,\sigma_y) + 6\psi^2(\sigma_x,\sigma_y))}{\psi(\sigma_x,\sigma_y)(3 - 2\psi(\sigma_x,\sigma_y))^2}
$$
$$
\cdot\,F_{sx}(\sigma_x,\sigma_y)F_{sy}(\sigma_x,\sigma_y) \quad (3.44)
$$

where (3.20) and (3.32) have been used in the last step.

$$
M_z''(\sigma_x, \sigma_y) = M_{az}''(\sigma_x, \sigma_y) + M_{sz}''(\sigma_x, \sigma_y) \quad (3.45)
$$

Finally,
$$
M_z(\sigma_x, \sigma_y) = M_z'(\sigma_x, \sigma_y) + M_z''(\sigma_x, \sigma_y) \quad (3.46)
$$

A commonly used parameter is the pneumatic trail, which denotes the distance between the center of the tire and point of action for the lateral force. It is defined as $t(\sigma_x, \sigma_y) = M_z(\sigma_x, \sigma_y)/F_y(\sigma_x, \sigma_y)$. The coordinate for the point of action for the adhesive force is denoted by

$t_a(\sigma_x, \sigma_y)$ and for the sliding force by $t_s(\sigma_x, \sigma_y)$. By using (3.39) and (3.20) respective (3.40) and (3.32) the contributions from $M'_z(\sigma_x, \sigma_y)$ to the pneumatic trail, $t'_a(\sigma_x, \sigma_y)$ and $t'_s(\sigma_x, \sigma_y)$, are given by

$$t'_a(\sigma_x, \sigma_y) = \frac{M'_{az}(\sigma_x, \sigma_y)}{F_{ay}(\sigma_x, \sigma_y)} = \frac{a}{3}(4\psi(\sigma_x, \sigma_y) - 1) \tag{3.47a}$$

$$t'_s(\sigma_x, \sigma_y) = \frac{M'_{sz}(\sigma_x, \sigma_y)}{F_{sy}(\sigma_x, \sigma_y)} = -3a\frac{(1 - \psi(\sigma_x, \sigma_y))^2}{(3 - 2\psi(\sigma_x, \sigma_y))} \tag{3.47b}$$

The contributions from $M''_z(\sigma_x, \sigma_y)$ can be read directly from (3.43) and (3.44).

In the same way as for the braking and cornering stiffness, the aligning stiffness is defined as

$$C_z = -\left.\frac{\partial M_z}{\partial \sigma_y}\right|_{\sigma_x, \sigma_y = 0} = c_{py}a^3\frac{2}{3} = C_y\frac{a}{3} \tag{3.48}$$

Analysis of the brush-model In Figures 3.8 and 3.9 the brush model is compared with the Magic Formula fitted to a truck tire. For the brush model also the combined-slip behavior is shown. The parameters are chosen so that the pure-slip curves have the same braking and cornering stiffnesses and the same peak force as of the Magic Formula. For the pure longitudinal slip the coherence between the brush model and the reference curve is good. For the pure lateral slip there are discrepancies in the lateral force and the self-aligning torque. The main reason for this is the assumption of a stiff carcass. This is realistic in the longitudinal direction, but for the lateral case where the carcass is weaker the effects of this simplification is noticeable. There exists more accurate models which include carcass flexibility based on assumptions on stretched string or beam behavior [Pacejka, 1988], see Section 4.4. The self-aligning torque also depends on the flexibility of the carcass which explains some of its disagreement to the measurements. Due to lack of data there were no possibilities to verify the deformation torque, M''_z, which probably is underestimated since only the rubber deformations are considered here.

A deficiency with the brush model is the assumption on velocity-independent sliding friction resulting in constant tire-forces at full sliding, which is obviously not correct as seen in e.g. Figure 3.8. Different

Figure 3.8   Tire forces as function of λ with $\alpha = [0, 5, 10, 20]$ deg. The dotted line shows the force from the adhesive region, the dashed line shows it from the sliding region. The solid line is the total force and the dashed dotted line is the reference curve created from a Magic Formula approximation of real tire data [Gäfvert and Svendenius, 2003]. For the self aligning torque the dotted line denotes the deformation torque M_z'' and the dashed line M'.

ways to introduce velocity dependence in the friction is discussed in Section 4.2. At partial sliding the approximation normally has small effects.

The LuGre Model

The LuGre model is known for describing special cases of friction situations and was developed as a joint cooperation between the Department of Automatic Control in Lund (Sweden) and in Grenoble (France) [Olsson, 1996]. The model describes a dynamic force phenomenon that arises when frictional surfaces are sliding on each other. The model
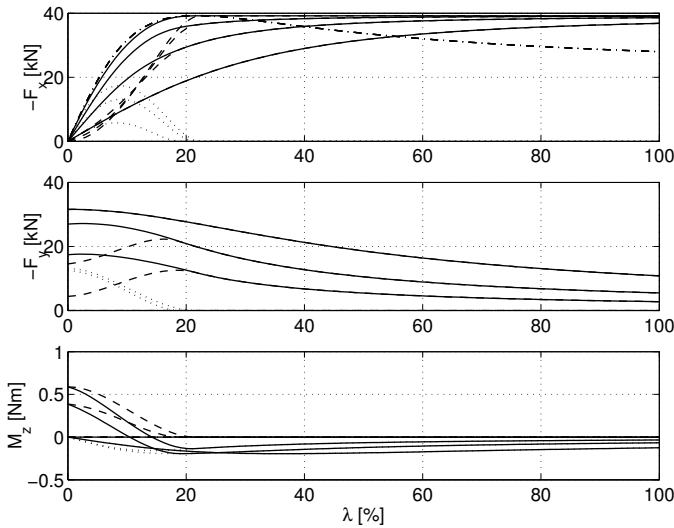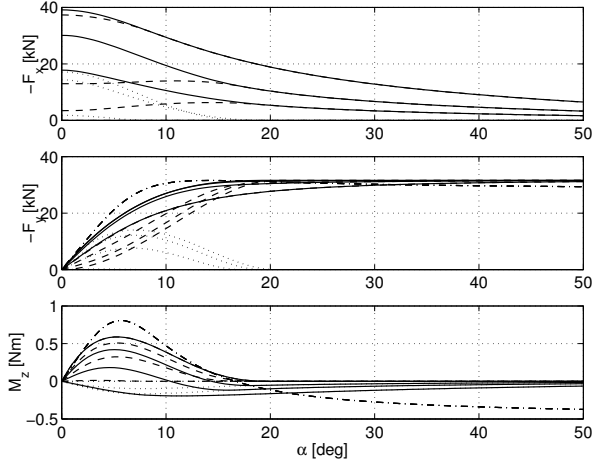
Figure 3.9 Tire forces as function of α with $\lambda = [0, 5, 10, 20]$ deg. The dotted line shows the force from the adhesive region, the dashed line shows it from the sliding region. The solid line is the total force and the dashed dotted line is the reference curve created from the Magic Formula. For the self aligning torque the dotted line denotes the deformation torque M_z'' and the dashed line M'.

is written on the form

$$\dot{z} = v_s - \frac{\sigma_0 |v_s|}{g(v_s)} z \tag{3.49a}$$

$$F_x = (\sigma_0 z + \sigma_1 \dot{z} + \sigma_2 v_s) F_z \tag{3.49b}$$

$$g(v_s) = \mu_k + (\mu_s - \mu_k) e^{-\sqrt{|v_s/v_{st}|}} \tag{3.49c}$$

where z is a state denoting deflection of the material in the friction surface. The friction, g($\cdot$) is assumed to be velocity dependent and the relation includes the static and kinetic friction coefficient, μ_s and μ_k respectively and the stribeck velocity, v_{st}. The material parameters are denoted by σ_i. The model was mainly aimed for describing friction in robot joints from the beginning. Later it has been introduced in the area of tire modeling [Canudas de Wit and Tsiotras, 1999] to describe the dynamic process when applying a torque on the tire. The contact patch is then, as the brush model divided into infinitesimal bristles,

41

but here supposed to behave according to (3.49a). The deflection $z(t)$ is extended to $z(x, t)$, denoting the bristle deflection at time t at the point x in the contact patch. The bristle deflection then corresponds to δ in Section 3.2. Since the bristle moves through the patch with the speed of the wheel v_c and $\dot{z}(x, t) = \frac{\partial z}{\partial t} + \frac{\partial z}{\partial x}\frac{\partial x}{\partial t}$ the LuGre model for the contact patch can be written as

$$\dot{z}(x, z) = \frac{\partial z}{\partial x}(x, t)|v_c| + \frac{\partial z}{\partial t}(x, t) = v_s - \frac{\sigma_0 |v_s|}{g(v_s)} z(x, t) \qquad (3.50)$$

$$F(t) = \int_{-a}^{a} (\sigma_0 z(x, t) + \sigma_1 \frac{\partial z}{\partial x}(x, t) + \sigma_2 v_s) f_z(x)\, dx \qquad (3.51)$$

The steady state solution for z with constant v_c and v_s can be calculated by setting $\frac{\partial z}{\partial t}(x, t) = 0$ and is given by

$$z^{ss}(v_s, v_c, x) = \frac{g(v_s)}{\sigma_0} \left(1 - e^{-\frac{\sigma_0}{g(v_s)}\left|\frac{v_s}{v_c}\right|x}\right) \qquad (3.52)$$

Figure 3.10 shows the steady state bristle deflection in the contact patch for the LuGre model at different slips. This could be compared to the brush model, see Figure 3.6, where the bristle deflection is proportional to the force working on a specific bristle illustrated by the marked area. In the brush model the pressure distribution limits the bristle deformation, but in the LuGre-model this limitation is included first in the force calculation (3.51). An analytical solution to (3.50) has not yet been presented, but even though it is numericly solvable it has to be simplified to allow practical use. Therefore, the lumped form has been introduced in the sense that the average bristle deformation, $\bar{z}(t)$ defined as

$$\bar{z} = \frac{1}{F_z} \int_0^L z(x, t) f_z(x)\, d\zeta \qquad (3.53)$$

is used as state variable. Then the dynamics of the system can be written as

$$\dot{\bar{z}} = \frac{1}{F_z} \int_0^L \frac{\partial z}{\partial t}(x, t) f_z(x)\, dx = v_s - \frac{\sigma_0 |v_s|}{g(v_s)} \bar{z}(t) - \kappa |v_c| \bar{z}(t) \qquad (3.54)$$
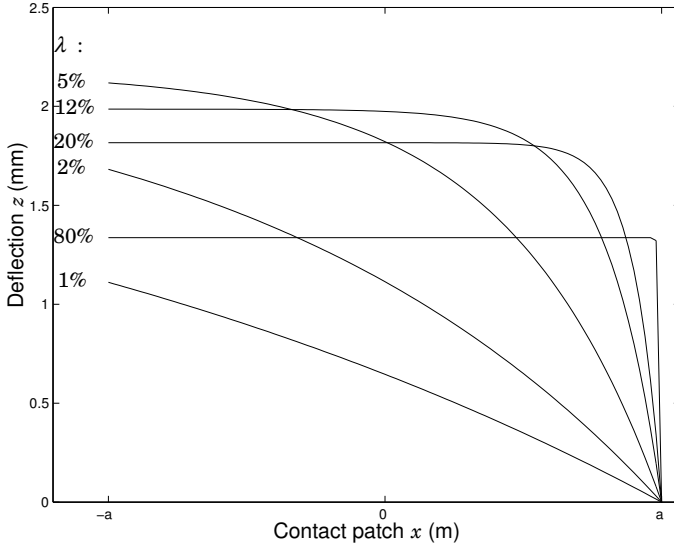
Figure 3.10 The steady state bristle deformation $z^{ss}(x)$ in the contact patch for different slip values λ. Note that $v_s = \lambda v$ and $v_c = v(1 - \lambda)$. The vehicle velocity, v is 60 kph and the length L of the contact patch is $2a = 0.15$ m.

Compared to (3.49a) only the term $-\kappa|v_c|\tilde{z}(t)$ is added, where

$$\kappa(t) = -\frac{\int_0^L z(t,x)f_z'(x)dx}{\int_0^L z(t,x)f_z(x)dx} \qquad (3.55)$$

The function $\kappa(t)$ has upper and lower bounds and depends of the choice on pressure distribution and the actual bristle deflection. It is descending with the upper bound $1/a$ at zero slip and zero as lower bound at high slips, assuming uniform distribution [Deur, 2002]. The effect of κ reduces at braking since the wheel velocity, v_c, then decreases. Therefore κ often is assumed to be constant with a value around its upper bound.

The lumped form is used in control and estimation issues, but when matching the σ-parameters to tune the model to experimental data the steady-state version of the distributed approach must be used.

The force corresponding to a certain slip is derived by insertion of z^{ss} from (3.52) into (3.51). Assuming constant vehicle velocity the steady-state force is only depending on the slip and can be written as

$$F_x^{ss}(\lambda) = \text{sign}(\lambda v) F_z g(\lambda v)$$
$$\cdot \left(1 + \left(1 - \frac{\sigma_1 |\lambda v|}{g(\lambda v)} \right) \frac{g(\lambda v)|1 + \lambda|}{\sigma_0 2a|\lambda|} \left(e^{-\frac{\sigma_0 2a|\lambda|}{g(\lambda v)|1+\lambda|}} - 1 \right) \right) + F_z \sigma_2 \lambda v \quad (3.56)$$

where $2a$ is the length of the contact patch. There are six parameters that has to be identified in this formula. In [Canudas de Wit and Tsiotras, 1999] it is claimed that it through parameter matching can get a shape very similar to the Magic Formula.

There exists an extension of the LuGre model into two dimensions with different properties in each direction. For the case of isotropic friction, the direction of the generated sliding force is opposite to the velocity vector and its magnitude independent of the heading of the sliding motion. Assuming anisotropic friction, the maximum dissipation principle (MDR) is generally used, see Section 3.2, which assumes that the friction force is build up so that maximal work is done. Maximal work means maximation of $W = v_s \cdot \mu$ where μ is limited by the friction ellipse, see Figure 3.5. In this context the resulting normalized friction force can written as

$$\mu^* = \frac{1}{\sqrt{\mu_{kx}^2 v_{sx} + \mu_{ky}^2 v_{sy}}} \begin{bmatrix} \mu_{kx}^2 v_{sx} \\ \mu_{ky}^2 v_{sy} \end{bmatrix} = \frac{M_k^2 v_s}{||M_k v_s||} \quad (3.57)$$

Since the LuGre model is a dynamic process and the movement of a bristle is the sum of its deformation and sliding it is necessary to distinguish between these two. For the sliding the MDR principle is used and for the elastic behavior the resulting force is collinear. The problem can be solved by the following Quasi-Variational Inequality (QVI)

$$-(\dot{u} + F_z K^{-1} \dot{u}^*)^T (\mu^* - \mu) \geq 0$$
$$\mu \in C = \{\mu \in R^2 : ||M_k^{-1} \mu|| \leq ||M_k^{-1} \mu^\star||\} \quad (3.58)$$

In [Velenis *et al.*, 2002] it is claimed that the QVI is fulfilled if the lumped form of the LuGre model is written on the following form for

two dimensions

$$\dot{\bar{z}}_i = v_{ri} - \frac{\sigma_{0i}\lambda(v_r)}{\mu_{ki}^2}\bar{z}_i - \kappa_i(t)|\omega r|\bar{z} \tag{3.59}$$

$$F_i = -F_n(\sigma_{0i}z_i(t) + \sigma_{1i}\dot{z}_i(t) + \sigma_{2i}v_{ri})), \ i = x, y \tag{3.60}$$

where

$$\lambda(v_s) = \frac{||M_k^2 v_s||}{g(v_s)} \tag{3.61}$$

and the friction function is redefined as

$$g(v_s) = \frac{||M_k^2 v_s||}{||M_k v_s||} + \left(\frac{|M_k^2 v_s|}{|M_k v_s|} - \frac{|M_k^2 v_s|}{|M_k v_s|}\right) \exp - \left(\frac{|v_s|^\gamma}{v_{st}}\right) \tag{3.62}$$

$$M_k = \left[\begin{array}{cc} \mu_{kx} & 0 \\ 0 & \mu_{ky} \end{array}\right] \quad M_s = \left[\begin{array}{cc} \mu_{sx} & 0 \\ 0 & \mu_{sy} \end{array}\right] \tag{3.63}$$

Then, the same procedure as for one dimension now has to be done for choosing the parameter values in the longitudinal and lateral direction. I.e. assume a pressure distribution, calculate the steady-state distributed bristle-deflection and integrate (3.51) over the entire contact patch. An optimization towards tire data then will give the parameter values. The derivation of κ has to be done in an different way, and more details on that and the procedure for deriving the self-aligning torque can be found in [Velenis *et al.*, 2002].

Discussion

In this section two ways to model the tire behavior have been presented. The models describe the physics quite differently even though they both depict the tire-force generation as sliding and deformation of bristles. The LuGre model requires six parameters in each of the two directions for good performance, but on the other hand enables good accuracy and flexibility for the steady state behavior and covers both dynamics and velocity dependency. The brush model as presented is described by only two parameters per direction, but includes neither velocity dependence nor dynamics. Inclusion of these entities is possible, see Section 2.2 and 4.2, and would require three additional parameters. However, in the following only the brush model is considered,

since it describes the physics in the most simplest form. It is possible to include further factors and describe additional effects and still keep the equations manageable. The LuGre model is a newer concept and the accuracy of, specially, its dynamic properties are not yet sufficiently documented.

3.3 Combined-Slip Semi-Empirical Tire Models

Pure-condition tire-forces may be described well by rather compact and simple empirical models that are widely accepted. Pure-slip tire data from test-bench experiments are often available for calibration. The situation for mixed conditions is somewhat different. The transition from one to two dimensions makes it more difficult to apply functional approximation. Empirical models tend to be either rough approximations or quite complex, difficult to understand, and rely on parameters that need to be calibrated with mixed-condition experimental data. This is a drawback since such data are only rarely available for a specific tire. Semi-empirical models uses the information from the pure-slip models to generate the tire forces when the vehicle brakes and turns simultaneously. Based on the mechanics of the tire and the available empirical data, a number of criteria for combined models may be stated (in the spirit of [Brach and Brach, 2000]):

1. The combined force $\bar{F}(\lambda, \alpha)$ should preferably be constructed from pure slip models $F_{0x}(\lambda)$ and $F_{0y}(\alpha)$, with few additional parameters.

2. The computations involved in the model must be numerically feasible and efficient.

3. The formulas should preferably be physically motivated.

4. The combined force $\bar{F}(\lambda, \alpha)$ should reduce to $F_{0x}(\lambda)$ and $F_{0y}(\alpha)$ at pure braking or cornering:

$$\bar{F}(\lambda, 0) = [\, F_{0x}(\lambda), 0 \,]$$
$$\bar{F}(0, \alpha) = [\, 0, F_{0y}(\alpha) \,]$$

5. Sliding must occur simultaneously in longitudinal and lateral directions.

6. The resulting force magnitudes should stay within the friction ellipse.

7. The combined force should be $\bar{F} = -F_z\mu\bar{v}_s/v_s$ at full sliding for tires with isotropic friction characteristics.

The most simplistic model of combined forces is based on the friction ellipse concept, see for instance [Wong, 2001; Ellis, 1994; Nielsen and Eriksson, 1999]. While the friction ellipse is the envelope of the maximum achievable forces, the ellipse is here used also for modeling intermediate forces. It is used to compute a combined lateral force $F_y(\alpha, \lambda)$ at a given longitudinal force F_x, and is based on the assumption

$$\left(\frac{F_x}{F_{0x}^*}\right)^2 + \left(\frac{F_y(\alpha, \lambda)}{F_{0y}(\alpha)}\right)^2 = 1 \tag{3.64}$$

where F_{0x}^* is the maximum achievable longitudinal force, and $F_{0y}(\alpha)$ the corresponding lateral force at pure slip

$$F_y(\alpha, \lambda) = F_{0y}(\alpha)\sqrt{1 - \left(\frac{F_x}{F_{0x}^*}\right)^2} \tag{3.65}$$

An objection to this model is the assumption (3.64), which is not true, since adhesion limits are not necessarily fully reached for combined forces in the interior of the friction ellipse.

Another simple model is the Kamm Circle [Kiencke and Nielsen, 2000], where the resultant force magnitude is described as a function of the total slip magnitude. The force and slip vectors are then assumed to be collinear, possibly with a corrective factor k_s:

$$F_x = F(s)\frac{s_x}{s} \qquad \text{and} \qquad F_y = k_s F(s)\frac{s_y}{s} \tag{3.66}$$

A drawback with this model is that longitudinal and lateral characteristics are assumed to be the same, modulo the corrective factor.

Some early efforts to model tire forces under combined-slip conditions are described and compared in [Nguyen and Case, 1975]. One of

the most well-known is presented in [Nicholas and Comstock, 1972]:

$$F_x(\lambda, \alpha) = \frac{F_x(\lambda) F_y(\alpha) \lambda}{\sqrt{\lambda^2 F_y^2(\alpha) + \tan^2(\alpha) F_x^2(\lambda)}} \tag{3.67a}$$

$$F_y(\lambda, \alpha) = \frac{F_x(\lambda) F_y(\alpha) \tan(\alpha)}{\sqrt{\lambda^2 F_y^2(\alpha) + \tan^2(\alpha) F_x^2(\lambda)}} \tag{3.67b}$$

In [Brach and Brach, 2000] this model is shown to give incorrect result for small slips and a modified version is presented.

In [Bakker *et al.*, 1987], a procedure for computing combined forces for the Magic Formula is presented. It is essentially a refinement of the Kamm Circle for non-isotropic tire characteristics and a normalization of the slips to guarantee simultaneous sliding. The normalized slip

$$\sigma_N = \sqrt{\left(\frac{\sigma_x}{\sigma_x^*}\right)^2 + \left(\frac{\sigma_y}{\sigma_y^*}\right)^2} \tag{3.68}$$

is an entity that is less than one for non-sliding conditions. It is based on an elliptic assumption where σ_x^* and σ_y^* are the longitudinal and lateral slips that corresponds to full sliding for pure slips, normally taken as the slips at the peak values F_{0x}^*, and F_{0y}^*. Now the combined forces are computed as

$$F_x = -\cos(\beta^*) F_{0x}(\sigma_x^* \sigma_N) \quad \text{and} \quad F_y = -\varepsilon_d(\sigma_N) \sin(\beta^*) F_{0y}(\sigma_y^* \sigma_N) \tag{3.69}$$

with $\tan(\beta^*) \triangleq \frac{\sigma_y/\sigma_y^*}{\sigma_x/\sigma_x^*}$. For large slip conditions the factor $\varepsilon_d(\sigma_N)$ must be included to give correct direction of the resulting forces. The reason is the fact that for small slips real tire-forces are essentially produced by elastic deformation, and for large slips by sliding friction. Therefore slip vectors of the same orientation but different magnitudes may result in forces with different orientation. It is not clear how to determine $\varepsilon_d(\sigma_N)$, and in [Bakker *et al.*, 1989] a modified procedure was presented:

$$F_x = \cos\left((1-\vartheta)\beta^* + \vartheta\beta\right) F_{0x}' \quad \text{and} \quad F_y = \sin\left((1-\vartheta)\beta^* + \vartheta\beta\right) F_{0y}' \tag{3.70}$$

with $\vartheta \triangleq \frac{2}{\pi} \arctan(q_1 \sigma_N^2)$ and

$$F_{0x}' \triangleq F_{0x}(\sigma_N) - \mathrm{sat}(\sigma_N) \left(F_{0x}(\sigma_N) - F_{0y}(\sigma_N)\right) \sin^2(\beta^*) \qquad (3.71\mathrm{a})$$

$$F_{0y}' \triangleq F_{0y}(\sigma_N) + \mathrm{sat}(\sigma_N) \left(F_{0x}(\sigma_N) - F_{0y}(\sigma_N)\right) \cos^2(\beta^*) \qquad (3.71\mathrm{b})$$

The variables ϑ, F_{0x}', and F_{0y}' describe the gradual change of orientation of the resulting force from adhesion to sliding. At large slip-magnitudes the force is collinear with the slip vector. In this new model only one parameter, q_1, is used.

In [Bayle *et al.*, 1993] a model for combined braking and cornering is presented, which is based on functional representation. The model is much inspired by the Magic Formula and uses functions based on arc tangents to describe forces under combined-slip conditions.

The recent COMBINATOR model [Schuring *et al.*, 1996; Pottinger *et al.*, 1998] is still a variation on the Kamm Circle. Here the tire force magnitude is described by

$$F = F_{0x}(s) \cos^2(\beta) + F_{0y}(s) \sin^2(\beta) \qquad (3.72\mathrm{a})$$

and the combined forces as

$$F_x = F \cos(\beta) \qquad \text{and} \qquad F_y = F \sin(\beta) \qquad (3.72\mathrm{b})$$

The model assumes collinearity between resulting force and the slip vector.

Much research has been devoted to semi-empirical tire-modeling and the brief survey above does by no means cover the area. Further references may be found in e.g. [Böhm and Willumeit, 1996].

3.4 A Novel Semi-Empirical Method Based on Brush-Tire Mechanics

This section presents a new model that combines empirical models for pure braking and cornering to a model for simultaneous braking and cornering, using a procedure based on brush-model tire mechanics, see Section 3.2. The approach is a result from a cooperation between the author of the thesis and PhD Magnus Gäfvert (LTH). Its most detailed description can be found in [Gäfvert and Svendenius, 2003].

Introduction

On a working tire the contact patch between the tire and the road is, in general, divided into an adhesive region where the rubber is gripping the road and a sliding region where the rubber slides on the road surface. The total force generated by the tire is then composed of adhesive as well as sliding force-components. The brush model describes these phenomena in a physical framework. In short, the proposed model is based on a method to extract the adhesive and sliding forces from pure-slip tire models. These forces are then manipulated to account for the combined-slip condition. The approach is quite different from most previous combined-slip models in that it is based on a rather detailed mechanical model in combination with empirical pure-slip models. The model does not rely on any additional parameters that depend on combined-slip data for calibration and is computationally sound and efficient. It does not depend on any specific pure-slip model, although in this work the Magic Formula is used for examples. Results show good correspondence with experimental data.

Generation of combined-slip forces

The general idea of the method to derive the forces at a combined slip (λ, α) is to scale the forces from the empirical pure-slip model at the certain pure slips $\lambda_0(\lambda, \alpha)$ and $\alpha_0(\lambda, \alpha)$. The pure slips can be chosen in various ways, but their relation to λ and α has to be well motivated and different proposals are discussed below. For convenience the arguments (λ, α) for λ_0 and α_0 are left out in the following. The scale factors depend on the current longitudinal and lateral slip and the relation between the used pure slip and the combined slip. Since the generation of forces from the adhesive and the sliding regions are built on different physical phenomena they are treated separately. The following equation, compare with (3.36), shows the form

$$\hat{F}_x(\lambda, \alpha) = G_{ax}(\lambda, \alpha)\hat{F}_{0x}(\lambda_{0a}) + G_{sx}(\lambda, \alpha)\hat{F}_{0x}(\lambda_{0s}) \tag{3.73a}$$

$$\hat{F}_y(\lambda, \alpha) = G_{ay}(\lambda, \alpha)\hat{F}_{0y}(\alpha_{0a}) + G_{sy}(\lambda, \alpha)\hat{F}_{0y}(\alpha_{0s}) \tag{3.73b}$$

where $\hat{F}_{0x}(\lambda_0)$ and $\hat{F}_{0y}(\alpha_0)$ are the forces from the empirical pure-slip model.

Scale factors

This section explains how the scale factors in (3.73a) are derived. Only the longitudinal direction is considered, but the procedure in the lateral direction is equivalent. As long as $F_{0ax}(\lambda_{0a}) \neq 0$ and $F_{0sx}(\lambda_{0s}) \neq 0$ it is possible to write

$$
\begin{aligned}
F_{ax}(\lambda, \alpha) &= \frac{F_{ax}(\lambda, \alpha)}{F_{0ax}(\lambda_{0a})} F_{0ax}(\lambda_{0a}) \\
F_{sx}(\lambda, \alpha) &= \frac{F_{sx}(\lambda, \alpha)}{F_{0sx}(\lambda_{0s})} F_{0sx}(\lambda_{0s})
\end{aligned}
\tag{3.74}
$$

To extract the adhesive and sliding forces from the empirical model the following rewriting is done

$$
\begin{aligned}
F_{0ax}(\lambda_{0a}) &= \frac{F_{0ax}(\lambda_{0a})}{F_{0x}(\lambda_{0a})} F_{0x}(\lambda_{0a}) \\
F_{0sx}(\lambda_{0s}) &= \frac{F_{0sx}(\lambda_{0s})}{F_{0x}(\lambda_{0s})} F_{0x}(\lambda_{0s})
\end{aligned}
\tag{3.75}
$$

Combination of (3.75) and (3.74) gives

$$
\begin{aligned}
F_{ax}(\lambda, \alpha) &= \frac{F_{ax}(\lambda, \alpha)}{F_{0x}(\lambda_{0a})} F_{0x}(\lambda_{0a}) \\
&= G_{ax}(\lambda, \alpha) F_{0x}(\lambda_{0a}) \approx G_{ax}(\lambda, \alpha) \hat{F}_{0x}(\lambda_{0a}) \quad (3.76)
\end{aligned}
$$

$$
\begin{aligned}
F_{sx}(\lambda, \alpha) &= \frac{F_{sx}(\lambda, \alpha)}{F_{0x}(\lambda_{0s})} F_{0x}(\lambda_{0s}) \\
&= G_{sx}(\lambda, \alpha) F_{0x}(\lambda_{0s}) \approx G_{sx}(\lambda, \alpha) \hat{F}_{0x}(\lambda_{0s}) \quad (3.77)
\end{aligned}
$$

Choice of Pure Slips and Derivation of Corresponding scale factor

The empirical pure-slip data include several effects which are not present in the theoretical brush-model. The most prominent are the mismatch of the lateral stiffness at partial sliding due to carcass flexibility and the apparent velocity dependence of the sliding friction. Still, the effects will be included in the proposed combined-slip model

as they essentially are scalings of the empirical data. In the special case of pure slip, these effects will be correctly reproduced. Otherwise, the different choices of pure-slips λ_0 and α_0 aim at reproducing particular effects correctly at combined-slip.

Adhesion region   The bristle deformations are the source of the adhesion forces. Therefore, for adhesion forces it makes sense to regard pure slips that result in the same deformation as the combined slip. The deformation state depends on the slip expressed in $\bar{\sigma} = (v_{sx}, v_{sy})/v_c$. The pure slip is therefore constructed to maintain $\bar{\sigma}$ constant. Translated to practical slip entities this means

$$\lambda_{0a} = \lambda \tag{3.78}$$

$$\alpha_{0a} = \arctan\left(\frac{\tan(\alpha)}{1 - \lambda}\right) \tag{3.79}$$

The scale factors G_{ax} and G_{ay} can now be calculated from the Equations (3.20), (3.33), and (3.35) together with the slip transformation in (2.6), as

$$G_{ax}(\lambda, \alpha) = \frac{F_{ax}(\lambda, \alpha)}{F_{0x}(\lambda_{0a})} = \frac{3\left(1 - \psi(\lambda, \alpha)\right)^2}{\Upsilon(\lambda_{0a}, 0)} \tag{3.80a}$$

$$G_{ay}(\lambda, \alpha) = \frac{F_{ay}(\lambda, \alpha)}{F_{0y}(\alpha_{0a})} = \frac{3\left(1 - \psi(\lambda, \alpha)\right)^2}{\Upsilon(0, \alpha_{0a})} \tag{3.80b}$$

with

$$\Upsilon(x, y) \triangleq \psi^2(x, y) - 3\psi(x, y) + 3 \tag{3.81}$$

if $\psi(\lambda, \alpha) < 1$ otherwise $G_{ax}(\lambda, \alpha) = G_{ay}(\lambda, \alpha) = 0$. For convenience, the normalized slip, ψ has been exposed to a slight redefinition. In this section holds

$$\psi(\lambda, \alpha) \triangleq \sqrt{\left(\frac{\lambda(1 - \lambda^\circ)}{(1 - \lambda)\lambda^\circ}\right)^2 + \left(\frac{\tan(\alpha)}{(1 - \lambda)\tan(\alpha^\circ)}\right)^2} \tag{3.82}$$

without this redefinition the expression above would be written as, $\psi(\sigma_x(\lambda, \alpha), \sigma_y(\lambda, \alpha))$. The designations, λ° and α°, are parameters to the model and will be further explained later on. In this section it is assumed that the sliding and the adhesive friction coefficient are equal, i.e. $\mu_{sx} = \mu_{kx}$ and $\mu_{sy} = \mu_{ky}$.

Sliding region   In the literature, slip-velocity is mentioned as a significant factor that influences the friction coefficient for a specific tire on a certain road foundation [Wong, 2001]. Therefore, it is reasonable to define the pure slip used for the sliding forces so that the slip velocity is invariant. The respective pure slips $(\lambda_{0s}, 0)$ and $(0, \alpha_{0s})$ at the wheel-travel velocity v_0, with

$$\lambda_{0s} = \frac{v}{v_0}\sqrt{(\lambda\cos(\alpha))^2 + \sin^2(\alpha)}\,\text{sgn}(\lambda) \tag{3.83a}$$

$$\sin(\alpha_{0s}) = \frac{v}{v_0}\sqrt{(\lambda\cos(\alpha))^2 + \sin^2(\alpha)}\,\text{sgn}(\alpha) \tag{3.83b}$$

result in the same slip velocity, v_s, as the combined slip (λ, α) at the wheel-travel velocity v. Note that v is the actual wheel travel velocity and v_0 the velocity at which the pure slip model is valid. The scaling factors G_{sx} and G_{sy} may then be computed from (3.20), (3.21), (3.35) and (3.32), using $\beta_f = \beta^-$ as

$$G_{sx}(\lambda, \alpha) = |\cos(\beta^-)| \cdot \Gamma_x \tag{3.84a}$$

$$G_{sy}(\lambda, \alpha) = |\sin(\beta^-)| \cdot \Gamma_y \tag{3.84b}$$

with

$$\Gamma_x \triangleq \begin{cases} \left(v_0\sqrt{1+\tan^2(\alpha)} - v\sqrt{\lambda^2+\tan^2(\alpha)}\,\text{sgn}(\lambda)\right)^2 \\ \cdot\dfrac{\Lambda^2\psi(\lambda_{0s},0)(3-2\psi(\lambda,\alpha))}{\Upsilon(\lambda_{0s},0)\tan^2(\alpha^\circ)v^2(1-\lambda)^2} & \text{if } \psi(\lambda_{0s},0) < 1 \\[2mm] \psi^2(\lambda,\alpha)(3-2\psi(\lambda,\alpha)) & \text{if } \psi(\lambda_{0s},0) \geq 1 \end{cases} \tag{3.85a}$$

and

$$\Gamma_y \triangleq \begin{cases} \left((v_0^2(1+\tan^2(\alpha)) - v^2(\lambda^2+\tan^2(\alpha)))\right)\Lambda^2(1-\lambda^\circ)^2 \\ \cdot\dfrac{\psi(0,\alpha_{0s})(3-2\psi(\lambda,\alpha))}{\Upsilon(0,\alpha_{0s})(v(1-\lambda)\lambda^\circ)^2} & \text{if } \psi(0,\alpha_{0s}) < 1 \\[2mm] \psi^2(\lambda,\alpha)(3-2\psi(\lambda,\alpha)) & \text{if } \psi(0,\alpha_{0s}) \geq 1 \end{cases} \tag{3.85b}$$

if $\psi(\lambda, \alpha) < 1$, otherwise

$$\Gamma_x \triangleq \begin{cases} \psi^{-1}(\lambda_{0s}, 0)\Upsilon^{-1}(\lambda_{0s}, 0) & \text{if } \psi(\lambda_{0s}, 0) < 1 \\ 1 & \text{if } \psi(\lambda_{0s}, 0) \geq 1 \end{cases} \tag{3.86a}$$

and

$$\Gamma_y \triangleq \begin{cases} \psi^{-1}(0, \alpha_{0s})\Upsilon^{-1}(0, \alpha_{0s}) & \text{if } \psi(0, \alpha_{0s}) < 1 \\ 1 & \text{if } \psi(0, \alpha_{0s}) \geq 1 \end{cases} \tag{3.86b}$$

$$\Lambda \triangleq \tan(\alpha^\circ)|\cos(\beta)|\cos(\beta^\circ) + \frac{\lambda^\circ}{1 - \lambda^\circ}|\sin(\beta)|\sin(\beta^\circ) \tag{3.87}$$

The friction-constraint angle β' can be derived from

$$\tan(\beta^-) = \begin{cases} \dfrac{\psi(0, \alpha_{0s})\Upsilon(0, \alpha_{0s})}{\psi(\lambda_{0s}, 0)\Upsilon(\lambda_{0s}, 0)} \dfrac{\tan(\alpha)}{\lambda} & \text{if } \psi(0, \alpha_{0s}) < 1 \\ (\psi(\lambda_{0s}, 0)\Upsilon(\lambda_{0s}, 0))^{-1}\dfrac{\tan(\alpha)}{\lambda} & \text{if } \psi(0, \alpha_{0s}) \geq 1 \end{cases} \tag{3.88a}$$

if $\psi(\lambda_{0s}, 0) < 1$ otherwise

$$\tan(\beta^-) = \begin{cases} \psi(0, \alpha_{0s})\Upsilon(0, \alpha_{0s})\dfrac{\tan(\alpha)}{\lambda} & \text{if } \psi(0, \alpha_{0s}) < 1 \\ \dfrac{\tan(\alpha)}{\lambda} & \text{if } \psi(0, \alpha_{0s}) \geq 1 \end{cases} \tag{3.88b}$$

and the normalized slip angle, β° as

$$\tan(\beta^\circ) \triangleq \frac{\psi(0, \alpha)}{\psi(\lambda, 0)} \tag{3.89}$$

Self-aligning Torque

For simplicity, another pure-slip definition is used for the self-aligning torque. The pure slips $(\lambda_0', 0)$ and $(0, \alpha_0')$, with

$$\lambda_0' = \frac{\lambda^\circ \psi(\lambda, \alpha)}{1 - \lambda^\circ + \lambda^\circ \psi(\lambda, \alpha)} \operatorname{sgn}(\lambda) \tag{3.90a}$$

$$\alpha_0' = \arctan(\tan(\alpha^\circ)\psi(\lambda, \alpha) \operatorname{sgn}(\alpha)) \tag{3.90b}$$

result in adhesion and sliding regions of the same size as the combined slip (λ, α). The pneumatic trail then remains unchanged as it only depends on the breakaway point, see (3.47a). The combined-slip self-aligning torque is given by

$$\hat{M}_z(\lambda, \alpha) = \hat{M}_{0z}(\alpha_0') |\sin(\beta')| + \Gamma_z \hat{F}_{0y}(\alpha_0') \qquad (3.91)$$

where

$$\Gamma_z = \frac{3(1 - \psi(\lambda, \alpha))^2}{\Upsilon(\lambda, \alpha)} t_a(\lambda, \alpha)(\sin(\beta^\circ) - |\sin(\beta')|) \qquad (3.92)$$

if $\psi(\lambda, \alpha) < 1$, otherwise $\Gamma_z = 0$, where $\Upsilon(\lambda, \alpha)$ is defined in (3.81), $t_a(\lambda, \alpha)$ as $C_z/C_y(4\psi(\lambda, \alpha) - 1)$, β° in (3.89), and β' in (3.88). The self-aligning torque consists of one adhesion and one sliding part, see (3.41), that are the product of the respective pneumatic trail and lateral force (3.47a). The sliding part of the empirical pure-slip torque is obtained by subtraction of the adhesive torque from the total torque as $\hat{M}_{0sz}(\alpha_0') = \hat{M}_{0z}(\alpha_0') - t_{0a}(\alpha_0')\hat{F}_{0ay}(\alpha')$, where $\hat{F}_{0ay}(\alpha')$ is given by $G_a'(0, \alpha')\hat{F}_{0y}(\alpha_0')$. The sliding force can be derived by using $F_{sy}(\lambda, \alpha) = G_s'(\lambda, \alpha)\hat{F}_{0y}(\alpha_0')$ and $F_{0sy}(\alpha') = G_s'(0, \alpha')\hat{F}_{0y}(\alpha_0')$, and the conversion between the combined slip and the pure slip keeps the size of the sliding region remained. Therefore $M_{sz}(\lambda, \alpha)$ can be computed by scaling $\hat{M}_{0sz}(\alpha_0')$ with $G_s'(\lambda, \alpha)/G_s'(0, \alpha')$. The adhesive part $M_{az}(\lambda, \alpha)$ is then added as $t_a(\lambda, \alpha)\hat{F}_{ay}(\lambda, \alpha)$. The scale factors G' can be derived from (3.76) and (3.77) using the above pure-slip definition.

Parameters

Only three additional parameters are needed in the model, which all have clear physical interpretations. The parameters λ° and α°, describe the pure slips where transition from partial to full sliding occur. They are needed to compute the normalized slip, $\psi(\lambda, \alpha)$. A common assumption is that these transitions occur when the tire forces obtain their maxima. Hence, the parameters may simply be set to the slip values corresponding to the maxima of $\hat{F}_{0x}$ and $\hat{F}_{0y}$. The parameter v_0 denotes the wheel-travel velocity for which the empirical pure-slip model is valid. The actual wheel-travel velocity v is assumed to be an input signal. If v_0 is not known then $v/v_0 = 1$ may be used, which will

neglect any velocity dependence. This is the common assumption in most other models.

Calculation of included parameters   The parameters, λ° and α° can be derived directly from the measurement data if the assumptions for the limit slips from the brush model are used. The force-peak values are given, as $\hat{F}_{0x}^*$, $\hat{F}_{0y}^*$ and the braking and cornering stiffnesses as $\hat{C}_\lambda$, $\hat{C}_\alpha$, the parameters λ° and α° may then conveniently be estimated as

$$\hat{\lambda}^\circ = \frac{3\hat{F}_{0x}^*}{3\hat{F}_{0x}^* + \hat{C}_\lambda} \tag{3.93a}$$

which follows from (3.17) and (2.6). Due to the flexibility in the carcass which is not included in the model this method does not perform well in the lateral direction. Instead, the following choice for $\hat{\alpha}_y^\circ$, derived in Section 4.4, is used

$$\hat{\alpha}_y^\circ = \arctan\left(\frac{2\hat{F}_{0y}^*}{C_\lambda} + \frac{\hat{F}_{0y}^*\pi}{C_\alpha\,180}\right) \tag{3.94}$$

The factor $180/\pi$ is due to α being expressed in degrees.

Automatic calculation of λ° and α° might be very useful when using a normal-load depending Magic-Formula pure-slip model. The parameters should then be calculated in every iteration using $\hat{F}_{0x}^* = (D)_x$, $\hat{F}_{0y}^* = (D)_y$, $\hat{C}_\lambda = (BCD)_x$ and $\hat{C}_\alpha = (BCD)_y$.

Results

Empirical data from a truck-tire (315/80R22.5) is used to exemplify the proposed model. The data is the same as been used in [Gäfvert and Svendenius, 2003] and is further presented there. It consists of pure-slip data with corresponding Magic Formula parameters. Pure-slip data for the lateral force and the self-aligning moment is only available for $|\alpha| < 20$ deg.

Combined slip examples   In Figure 3.11, the resulting forces and aligning moments are shown for fixed slip-angles and varying slip-ratio, ranging from 0 to 100% (braking with locked wheels). The adhesion and sliding contributions are shown separately for the forces and
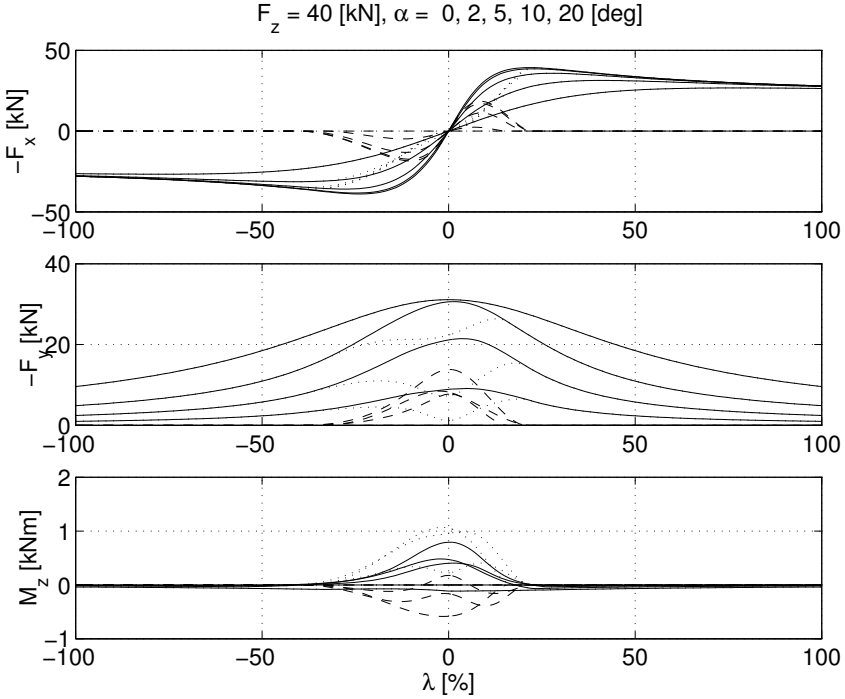
Figure 3.11   Combined-slip forces for fixed α, as λ is swept from -100% (driving) to 100% (braking with locked wheels). Top: F_x (solid), F_{ax} (dotted), F_{sx} (dashed). Middle: F_y (solid), F_{ay} (dotted), F_{sy} (dashed). Bottom: M_z (solid), M_{az} (dashed), M_{sz} (dotted).

the torque. The adhesion force is dominating at small slip magnitudes and vanishes at the point of full sliding. Note the asymmetrical characteristics with respect to driving ($\lambda < 0$) and braking ($\lambda > 0$). This is, essentially, an effect of using the deformation invariant pure slip for the adhesion forces. The combined-slip forces and moments agree qualitatively well with observations reported in e.g. [Pacejka, 2002]. Figure 3.12 shows the corresponding case with fixed slip ratio, as the slip angle is swept from 0 to 30 deg. Negative slip angles are not shown since the characteristics are symmetrical. For small slips, the direction
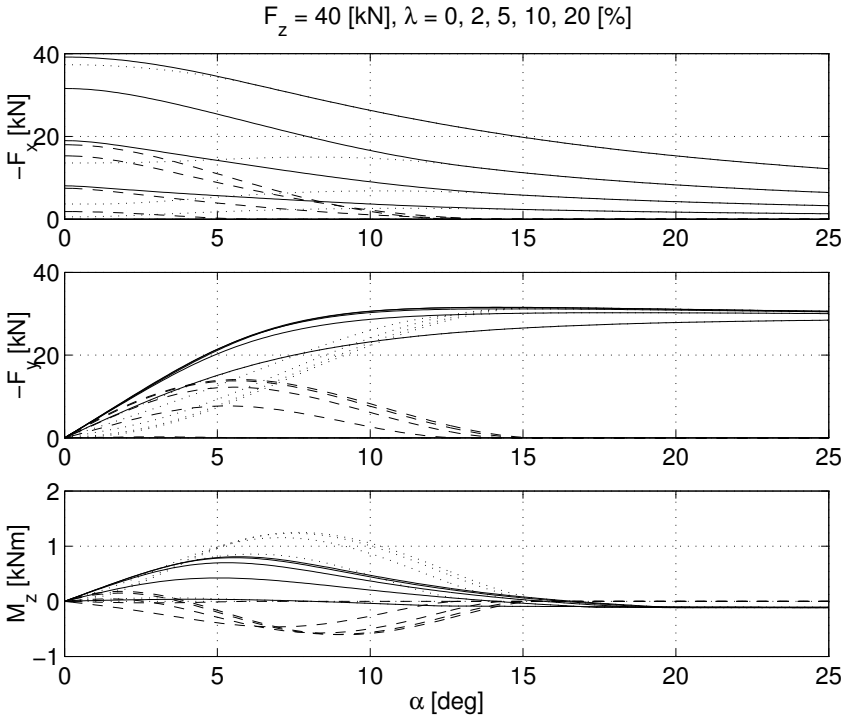
F_z = 40 [kN], λ = 0, 2, 5, 10, 20 [%]

Figure 3.12   Combined-slip forces for fixed λ, as α is swept from 0 to 25 deg. Top: F_x (solid), F_{ax} (dotted), F_{sx} (dashed). Middle: F_y (solid), F_{ay} (dotted), F_{sy} (dashed). Bottom: M_z (solid), M_{az} (dashed), M_{az} (dotted).

of the tire-force is, primarily, determined by the stiffness characteristics of the tire. For larger slips, when the sliding friction dominates, the force is collinear with the slip vector. This gradual change in orientation of the force with increasing slips is an important feature of the model. This can be seen more clearly in the figures below.

Validation   The model was validated with two sets of combined-slip data for fixed slip-angles, $\alpha = 4.7$ deg and $\alpha = 9.8$ deg, with varying slip ratios, λ, in the range 0–100%. These measurement sets were collected together with the pure-slip tire-data used earlier. The model

responses are shown together with the combined-slip measurements in Figure 3.13. The model clearly captures the main combined-slip behavior. Deviations result from the simplifications that are used in the model, but also in difficulties in the experimental procedure for collecting the empirical data. Some obvious anomalies in the data are found at the end points. The combined-slip lateral forces at $\lambda = 0\%$ does not agree with the corresponding force in the pure-slip data set. The combined-slip force vectors at full sliding ($\lambda = 100\%$) are difficult to explain. They do not agree with the assumption on collinearity with the slip vectors, or any other reasonable assumptions, see Section 3.2.

Velocity dependence   The dependence on wheel-travel velocity is illustrated in Figures 3.14 and 3.15, by varying the ratio v/v_0. The pure-slip Magic-Formula model is calibrated with data from tire measurements at the wheel-travel velocity v_0.[1] Tire forces are shown for velocities that are 1–4 times the wheel-travel velocity of the pure-slip model. The results agree qualitatively well with what is reported in e.g. [Pacejka, 2002]. The slip velocity at a combined slip (λ, α), is $v_s = v \left(\lambda^2 \cos^2(\alpha) + \sin^2(\alpha) \right)^{1/2}$. Corresponding pure slips for the empirical pure-slip model are given by $v_s = \lambda_{0s} v_0$ and $v_s = \sin(\alpha_{0s}) v_0$. These expressions can be solved for pure slips $\lambda_{0s} < 100\%$ and $\alpha_{0s} < 90$ deg, when $(v/v_0)^2 \left(\lambda^2 \cos^2(\alpha) + \sin^2(\alpha) \right) \leq 1$, see (3.83). If instead $(v/v_0)^2 \left(\lambda^2 \cos^2(\alpha) + \sin^2(\alpha) \right) > 1$, which may occur only if $v/v_0 > 1$ or α_{0s} is outside the valid range of the pure-slip model, then extrapolation is necessary. A straightforward method is to use the end points of the models. The Magic Formula with default shape factor has decent extrapolation properties and may be used with slip ratios $\lambda_{0s} > 100\%$. In general, extrapolation of empirical data must be carried out with great care.

Relations to other models   Figure 3.16 is similar to Figure 3.13 and shows the combined forces at constant slip angles, as the slip ratio is swept from -100% to 100%. In Figure 3.16, comparisons are shown between the proposed model, the BPL model [Bakker *et al.*,

---

[1]The exact value of v_0 is not known for this data. Measurements are normally performed at around 10 m/s on the used test-bed.
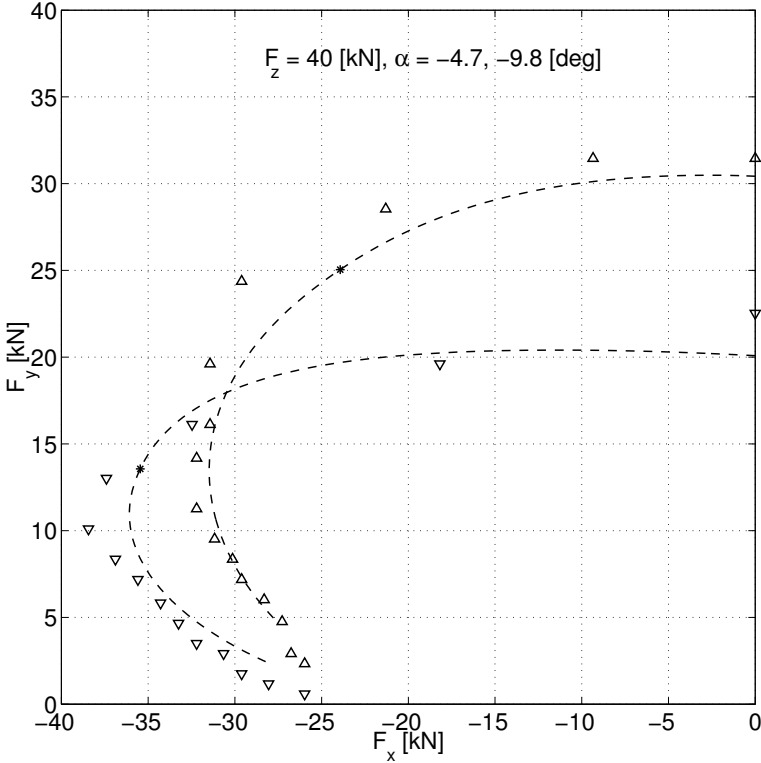
Figure 3.13 Comparison between the proposed combined-slip model (dashed) and combined-slip measurements for $\alpha = 4.7$ deg (triangle down) and $\alpha = 9.8$ deg (triangle up), as λ is swept from 0 to 100%. Transition to full sliding $\psi(\lambda, \alpha) = 1$ is marked by an asterisk

1989], and the COMBINATOR model [Schuring *et al.*, 1996]. In the COMBINATOR model the resulting force is always collinear with the slip vector, which is an assumption with weak physical motivation. Also the lateral force initially increases, as a longitudinal slip is applied. This is a result of the assumption of a collinear combined-slip tire-force in the full slip range, in combination with the use of the magnitude of the combined-slip slip-vector in the empirical pure-slip models.

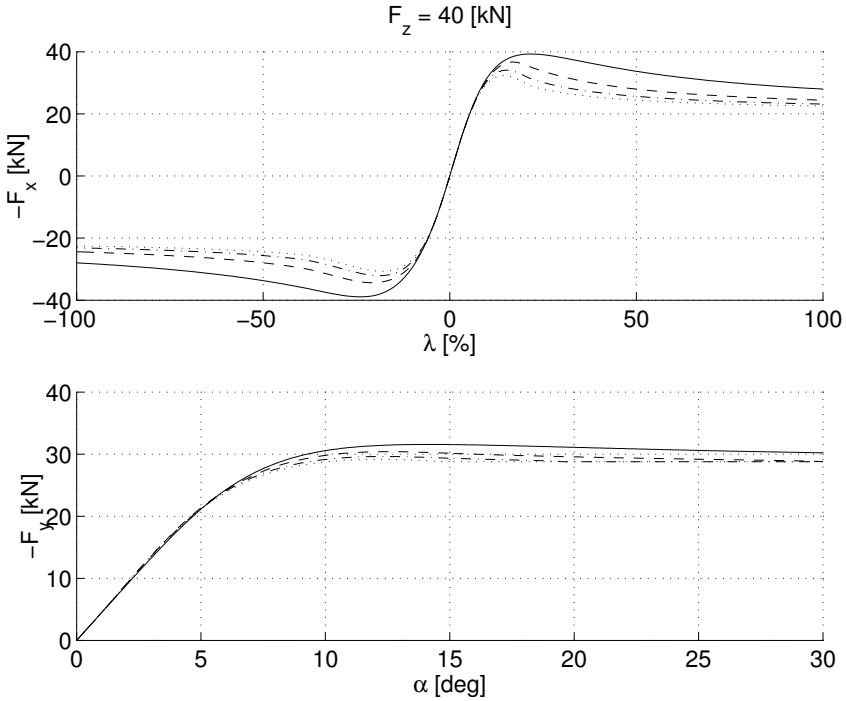In [Gäfvert and Svendenius, 2003] it is shown that the proposed

Figure 3.14   Velocity dependence at pure slips. Velocities: $v = v_0$ (solid), $2v_0$ (dashed), $3v_0$ (dash-dotted), $4v_0$ (dotted).

model with a pure slip based on region invariance, (3.90), is very similar to the BPL model. One major reason for this is that also the BPL model uses the region-invariant pure slips.

Conclusions

This section has presented a new method to derive the tire forces for simultaneous braking and cornering, by combining empirical models for pure braking and cornering. The proposed model is based on understanding of the physical sources of tire forces, as given by the theoretical rigid-carcass brush-model. Based on the brush model, the combined-slip forces may be described by a scaling of corresponding
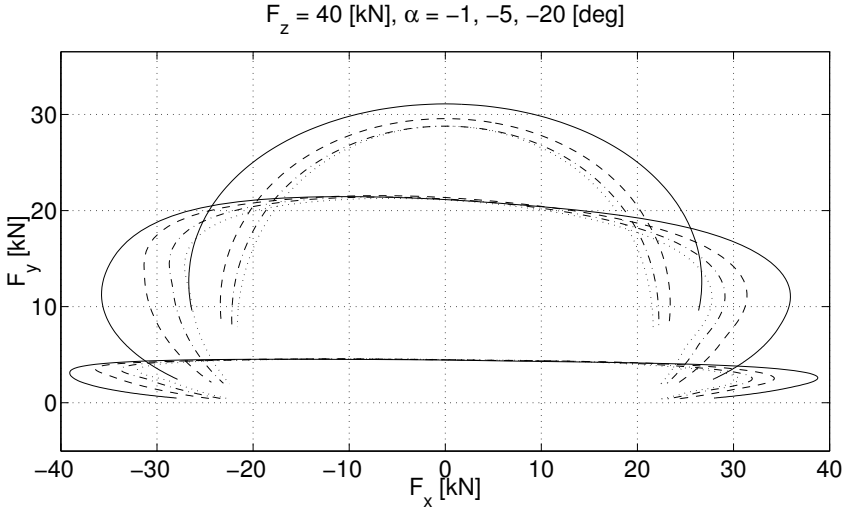
Figure 3.15   Velocity dependence at combined slips. Velocities: $v = v_0$ (solid), $2v_0$ (dashed), $3v_0$ (dash-dotted), $4v_0$ (dotted).

empirical pure-slip forces. There is a freedom in choosing the pure-slip forces, which may be used to emphasize different physical effects. This made it easy to include velocity dependence in the model, in a unique way. The model is simple since the included parameters can be derived automaticly. This is a feature allowing continuous changes in the pure slip models during simulation. All necessary information is given by the used pure-slip model. The stated criteria in Section 3.3 concerning the behavior of a combined slip model is fulfilled, using this method.

Even though the model in its present state is useful for a number of applications, the addition of effects of camber and flexible carcass might be necessary to increase the applicability even more. The physical foundation of the model is expected to make this possible with reasonable effort.

Good results are obtained in validation with empirical data. Relations to similar, previously published combined-slip models are analyzed. Previous models are partly heuristically based, while the proposed model is entirely based on physical principles. It is concluded
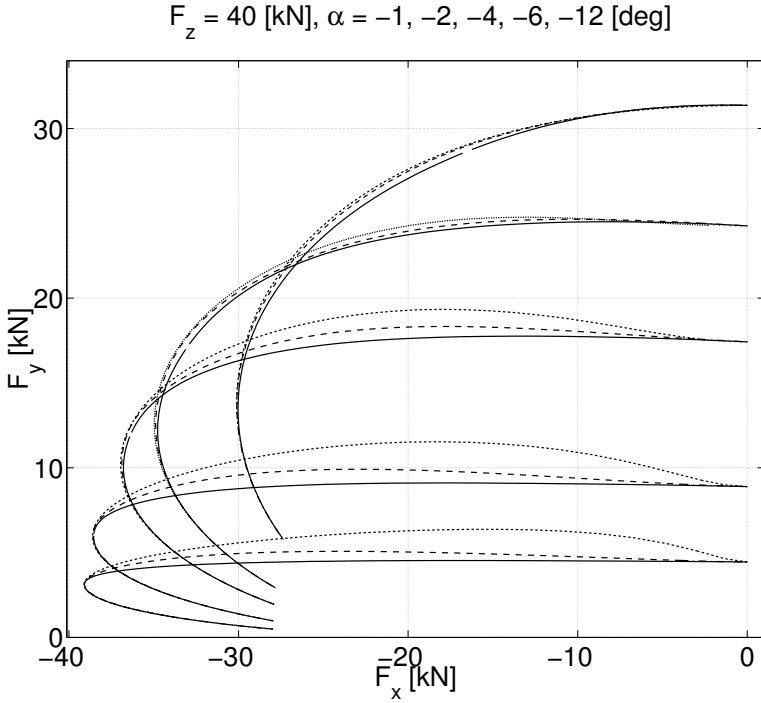
Figure 3.16   Combined-slip forces with the proposed model for fixed slip angles α and varying λ ranging from 0 to 100% (braking with locked wheels). The COMBINATOR model (dotted) and the BPL model (dashed) are shown for comparison.

that the suggested model is more accurate than the COMBINATOR model [Schuring *et al.*, 1996]. The BPL model [Bakker *et al.*, 1989] show similar agreement. None of these previous models include velocity dependence.

4

Details of the Brush Model

4.1 Vertical Pressure Distribution

Vertical Deformation Pressure Distribution

Exposed to a vertical load the tire will deform. An exact analysis of the deformation requires good calculation tools and accurate information about the tire design and actual conditions, as axle load, road surface, and temperature. Schematicly, the deformation can be divided into two parts. One part from the change of the carcass shape and one from the compression of the rubber material. If the carcass deformation is moderate the air volume in the tire will remain nearly constant and no consideration to increased tire pressure is necessary. In the static case, i.e. when the wheel is not rolling, the maximal pressure between the tire and the road, normally, can not exceed the pressure inside the tire, p_0. There is an area in the center of the contact patch where the pressure is equal to p_0. In the outer region where the carcass lifts from the ground the compression of the rubber gives a smooth transition of the pressure from p_0 to 0, where the contact area ends. The pressure distribution in a longitudinal cut of the tire then might look as the example shown in Figure 4.1. In the lateral direction the distribution depends on shape of the carcass. An laterally arched carcass, which corresponds to a well-inflated tire, gives a round contact patch.
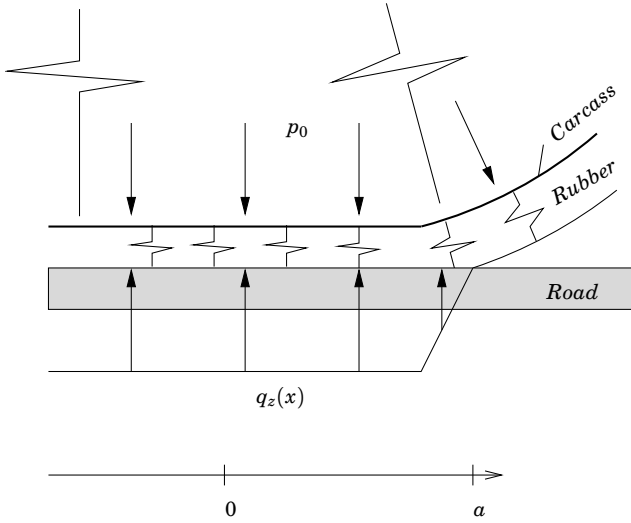
Figure 4.1 Illustration of the vertical pressure distribution in a longitudinal cut of the tire. Note that $q_z(x) = p_0$ in the major part of the cut.

A poorly inflated tire results in a more flat carcass, which gives a more rectangular patch. In Figure 4.2 these two different special cases are shown and any intermediate solution is realistic. In the first case it is assumed that the contact zone has a shape of a circle or ellipse, with the area $A = \pi ac$. There is a linear relation between a and c and using $F_z \approx p_0 A = k_0 a^2$ makes the contact length a proportional to $\sqrt{F_z}$. In the second case where $A = 4ab$, a is instead linear to F_z. Note that if only the solid line in the figure moves when the vertical force changes, A will remain constant for different values of F_z. Therefore it is a difficult task to find an relation between a and F_z. An example of the pressure distribution is shown to the left in Figure 4.3 for a non-rolling tire. For the dynamic case it is different. The movement of the wheel changes the appearance of the pressure distribution and it will no longer be symmetric. When the wheel is rotating it deforms continuously and a braking torque called rolling resistance is developed. The pressure increases in the front half of the contact patch and
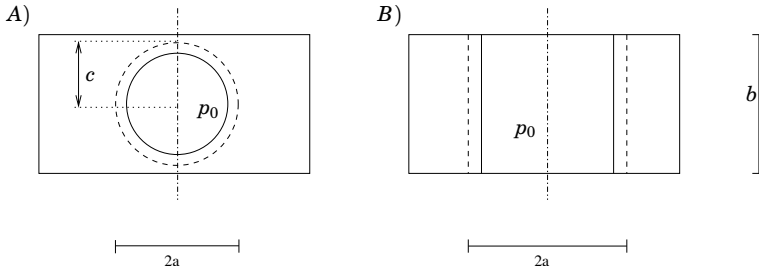
A)   B)

Figure 4.2   Illustration of the tire contact patch (top view). Inside the solid lines the pressure is p_0, then it decreases to zero at the dashed line. A) Well-inflated tire; B) Poorly inflated tire.
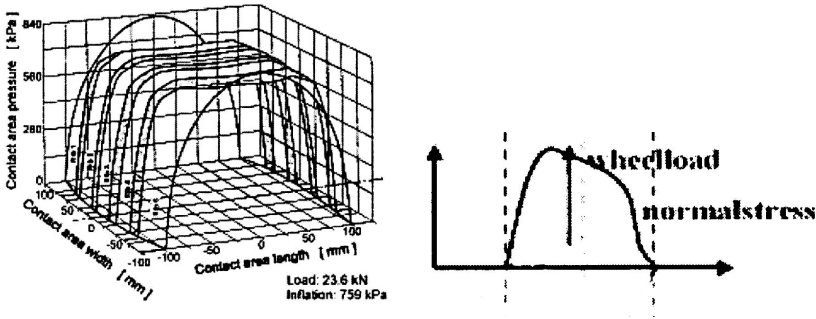
Figure 4.3   Example of vertical pressure distribution. To the left it is shown for the whole contact patch of a non-rolling tire and to the right only the lateral average is shown for a rolling tire. Rolling direction is leftwise in the right figure. Reprinted from [Pauwelussen *et al.*, 1999].

decreases in the rear half. The amount of the change is depending on the velocity, the damping, and the mass of the deformed material. How a braking/driving or cornering force changes the pressure distribution is not obvious. In general, the center for the vertical force moves in the opposite direction as the generated tire force is working [Wong, 2001]. When the pressure distribution is used further in the paper, it is laterally lumped, i.e. the lateral average is calculated. The pressure

distribution in N/m is then given as a function of the longitudinal coordinate x.

Pressure Distribution

The brush tire model described in Section 3.2 uses parabolic pressure distribution between the tire and the road. In this chapter different distributions are introduced and their effect on the force-slip relation is examined. The second proposal is an asymmetric third order approach with an extra parameter which moves the top of the curve and changes the asymmetric properties. The third curve is symmetric and defined by a forth order formulation. All equations are scaled so that the resulting force will be equal to F_z. The distributions are only defined in the longitudinal direction and supposed to be the average value of the distribution in the lateral direction. The parabolic pressure distribution used in Section 3.2 is denoted q_{z1} and given by (3.14). The resulting force assuming only longitudinal movements and constant friction $(\mu_s = \mu_k)$ can be written

$$F_{0x} = C_x\sigma_x - \frac{1}{3}\frac{(C_x\sigma_x)^2}{\mu F_z} + \frac{1}{27}\frac{(C_x\sigma_x)^3}{(\mu F_z)^2} \tag{4.1}$$

for $\sigma_x < \sigma_x^\circ$, otherwise $F_{0x} = \mu F_z$. The asymmetric distribution is given by

$$q_{z2}(x) = \frac{3F_z}{4a}\left(1 - \left(\frac{x}{a}\right)^2\right)\left(1 + d\frac{x}{a}\right) \tag{4.2}$$

and the expression for the symmetric forth order pressure curve is

$$q_{z3}(x) = \frac{5F_z}{8a}\left(1 - \frac{x^4}{a^4}\right) \tag{4.3}$$

The curves are visualized in Figure 4.4. In (4.2) it possible to move the point of the maximal pressure to the left or to the right by changing d. To avoid negative pressure values inside the contact patch the parameter must stay in the range of $|d| < 1$. A discussion about the shape of the contact patch and the pressure distribution is performed previously and the special case with a circular patch as to the left in Figure 4.2 with a very small transition region the lumped pressure

distribution would have an elliptic shape ($q_z = k_0\sqrt{1-(x/a)^2}$). Allowing a larger transition region the curve close to $x = \pm a$ will decrease. Probably, $q_{z1}(x)$ then is a realistic assumption. For the second case in Section, where the contact patch is more rectangular, $q_3(x)$ is a better choice. For these static cases the vertical pressure may not exceed the tire pressure. When the wheel rolls the continuous deformation of the tire changes the pressure distribution. The damping together with the mass forces increases the pressure at the leading side and decrease it on the trailing side. There might also be some effects from the centrifugal forces caused by the wheel rotation. The asymmetric third order function, $q_{z2}(x)$, with a positive d is then a realistic choice. When a tire force is applied the carcass deforms and the center of the pressure distribution even further. The parameter d could then even reach negative values. A correct choice of pressure distribution needs a lot of further investigation and measurements. Later on we will see how different distributions affects the force-slip curve and that the choice of it might not be done on theoretical foundations.

Force-slip function for an asymmetric pressure distribution.

The pressure distribution $q_{z1}(x)$ is now replaced by q_{z2} and by eliminating the root $x_s = a$ from (3.15) and restrict to only longitudinal motions the breakaway point can be derived by

$$\frac{3\,F_z\mu}{4\,a^2}\left(1+\frac{x}{a}\right)\left(1+d\,\frac{x}{a}\right) = c_p\sigma_x \tag{4.4}$$

with the solutions

$$x_s = -\frac{a}{2d}(d+1) \pm \frac{a}{2d}\sqrt{(d-1)^2 + \frac{8\,C_x d}{3\mu F_z}\sigma_x} \tag{4.5}$$

To be able to use the calculation scheme from Section 3.2, one and only one solution can be inside the contact region. Therefore the sign in front of the square root has to be positive. For d less than -0.5 there are two solutions inside the interval. Physically it means that there are two sliding areas split by one adhesive region. To avoid that, the interval for d is restricted to $[-0.5, 1]$. The total brake force, which
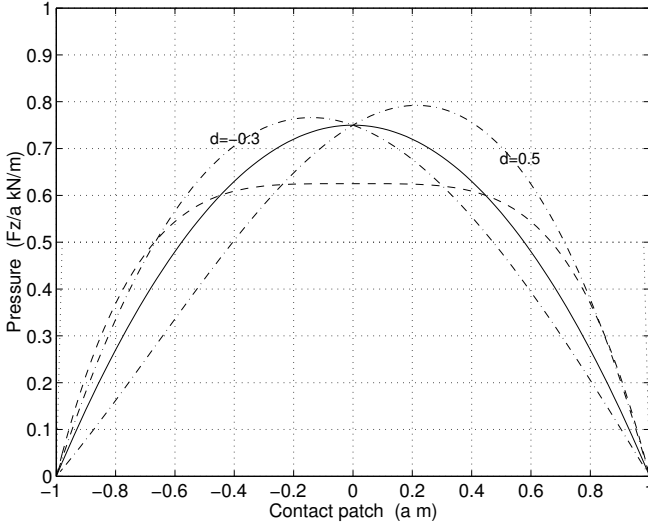
Figure 4.4   The pressure distributions proposed in this chapter. The wheel is supposed to move to the right. The leading side will then be to the right and the trailing side is accordingly to the left. the solid line shows pressure distribution according to Equation (3.14), dashed line according to (4.3) and the dashed dotted ones to Equation (4.2) with different choices on d.

can be derived using (3.11) and (3.23) is given by

$$F_{0x} = \frac{\mu F_z}{32d^3}(1-d)^3(3d+1) + \frac{C_x}{8\,d^2}(2\,d+5\,d^2+1)\sigma_x$$
$$+ \frac{1}{6}\frac{C_x^2\,\sigma_x^2}{\mu\,F_z\,d} - \left(\frac{\mu F_z}{32d^3}(d-1)^2 + \frac{C_x}{12\,d^2}\right)(3\,d+1)\sigma_x$$
$$\cdot\sqrt{(d-1)^2 + \frac{8\,d\,C_x\sigma_x}{3\mu F_z}}\quad(4.6)$$

The slip limit where the entire contact area slides towards the ground is given by the incline of the pressure curve in $x = a$. Hence,

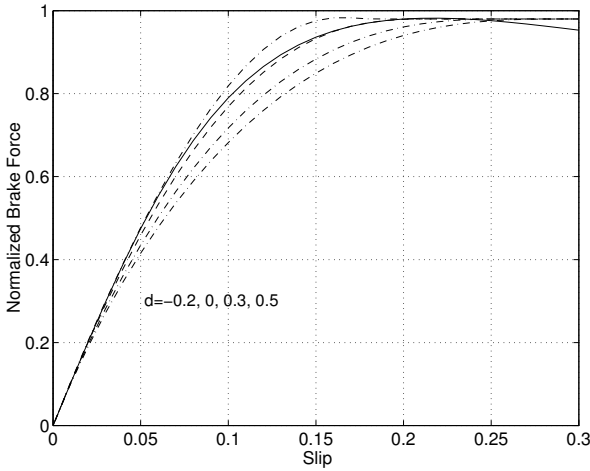$$F_x = \mu F_z \quad \text{if} \quad \sigma_x > \frac{3\mu F_z}{C_x}(1+d)\qquad(4.7)$$

Figure 4.5   Illustration showing the brake force contra the slip using the pressure distribution given by (4.2). The solid line denotes a Magic Formula realization from a real tire. The others are derived using different value of d.

The result for some different values of d is shown in Figure 4.5. The complexity of (4.6) could be reduced by choosing d to 1 or $-1/3$. However, the idea to change the pressure distribution in this way is to get a calibration parameter that can be changed continuously.

Symmetric fourth order pressure distribution   The same procedure as above can be done for the pressure distribution described by (4.3). There is no extra parameter introduced in this approach and yet the expression for the solution gets too complex to be presented. The shape of the resulting force-slip curve, which is shown in Figure 4.6, shows the difference using the fourth order distribution.

Discussion   The results from the alternative brush models have so far only been compared to one Magic Formula estimation. The Magic Formula is probably the best way to approximate measurement data by an expression. However, it might not exactly cover the truth tire characteristic and also different tire differ from each other. Therefore,
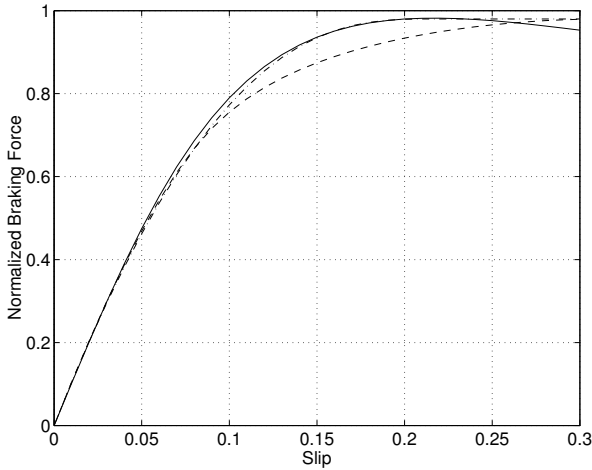
Figure 4.6 Brake force contra slip. The solid line denotes a Magic Formula optimized from real data. The dashed line is derived form the fourth order pressure distribution and the dashed-dotted from the non-compensated brush model.

it could be dangerous to draw too many conclusions just from this reference curve. There are also other factors than the pressure distribution that can affect the shape of the curve. Having that in mind we say that the fourth order curve matches very well at slip up to 70% of the maximal brake force. This means that the distribution is realistic at the trailing side, but the pressure should decrease faster when reaching the leading end. The parabolic pressure distribution give a good overall fit to the Magic Formula approximation. However, choosing the asymmetric curve with a slightly negative d gives better accuracy for slip up to 0.07, even though it has some mismatch at higher brake forces. That implies that the top of the pressure distribution should be a little bit behind the the center of the contact patch. It could also imply that d and the peak moves with the achieved brake force, which is reasonable. Then the d-value should be changed depending on the load and brake force.

4.2 Velocity Dependent Friction

Another way to increase the flexibility of the brush tire model is to introduce a sliding-velocity dependent friction coefficient. The bristles in the contact patch are assumed to slide against the road with the velocity $v_{sx} = v_x \sigma_x / (\sigma_x + 1)$ directly after passing the breakaway point x_s, see Figure 3.1.

Three different cases of velocity dependence are treated in the following. First, in the meaning that the friction is constant but has different value whether the bristles are gripping or sliding on the road. The value μ_s denotes the static friction and μ_k, the kinetic. In the second case the friction coefficient is linearly dependent on the sliding velocity. Finally, an exponential relation between the friction and the sliding velocity is assumed. The two last cases are examined in two ways. Either, only the kinetic friction will be velocity dependent and the static coefficient constant or both the static and the kinetic friction have the same velocity dependence.

Constant Friction

The friction is in this case assumed to be constant, but having different values whether the bristles are sliding or gripping the road. Referring back to Section 3.2 and solving Equation (3.15) assuming only longitudinal motions, gives the position for the break-away point as

$$x_s = \frac{1}{3} \frac{a\,(2 C_x\,\sigma_x - 3\,\mu_s\,F_z)}{\mu_s\,F_z} \tag{4.8}$$

Evaluating (3.36) where μ is changed to μ_k gives

$$F_{0x} = C_x\,\sigma_x + \frac{1}{3} \frac{C_x^2\,(\mu_k - 2\,\mu_s)\,\sigma_x^2}{F_z\,\mu_s^2} + \frac{1}{27} \frac{C_x^3\,(3\,\mu_s - 2\,\mu_k)\,\sigma_x^3}{F_z^2\,\mu_s^3} \tag{4.9}$$

For $\sigma_x > \sigma_x^\circ = 3\mu_s F_z / C_x$ the entire surface slides and the brake force is given by

$$F_{0x} = \mu_k F_z$$

A difference between this realization and the one from Section 3.2 is that the top of brake force curve is reached for a lower slip than total

sliding occurs. By differentiating (4.9) and locating the zeros, the slip value that corresponds to the peak force can be derived. Since (4.9) is a third order equation two zeros are obtained. One belonging to the maximal force, σ_x^* and one belonging to the slip where the total sliding starts, σ_x°. The slip, where the force has its maximum, is given by

$$\sigma_x^* = \frac{3\mu_s^2 F_z}{C_x\,(3\mu_s - 2\mu_k)} \tag{4.10}$$

with the corresponding peak force

$$F_{0x}^* = \frac{(4\mu_s - 3\mu_k)\mu_s^2}{(3\mu_s - 2\mu_k)^2} F_z \tag{4.11}$$

The calibration factor m is introduced such that the shape of the force/slip curve can be adjusted for given braking stiffness and peak brake force. Define $m = \mu_k/\mu_s$ and the static friction can be expressed by $\mu_s = F_{0x}^*(3 - 2m)^2/(F_z(4 - 3m))$ for $m \in [0, 1]$. In Figure 4.7 the force-slip curve is plotted for some different values of m. The expression for the force including the parameter m and $\mu' = F_{0x}^*/F_z$, for $\sigma_x \leq 3\mu_s/(2c_p a^2)$ is

$$F_{0x} = C_x\,\sigma_x + \frac{1}{3}\frac{C_x^2\,(m - 2)(4 - 3m)}{F_z\mu'(3 - 2m)^2}\sigma_x^2 + \frac{1}{27}\frac{C_x^3}{(F_z\mu')^2}\frac{(4 - 3m)^2}{(3 - 2m)^3}\sigma_x^3 \tag{4.12}$$

Linear Velocity Dependency

To include velocity dependence on the friction, any relation $\mu_k = f_k(v_s)$ and $\mu_s = f_s(v_s)$ can be put into (4.9). If both friction coefficients are assumed to depend on the slip velocity in the same way $\mu = f(v_s)$ can be put into (4.1). Recall that v_s is the relative velocity between the tire carcass and the road. The entire sliding part in the contact patch is assumed to slide with v_s. Since the work is restricted to only longitudinal movements $v_s = v_{sx}$ and the velocity of the vehicle $v=v_x$ and v_{sx} can be expressed as $\kappa_x v_x$ according to Equation (2.5). The expressions have to be dependent on σ_x instead of κ_x so the transform
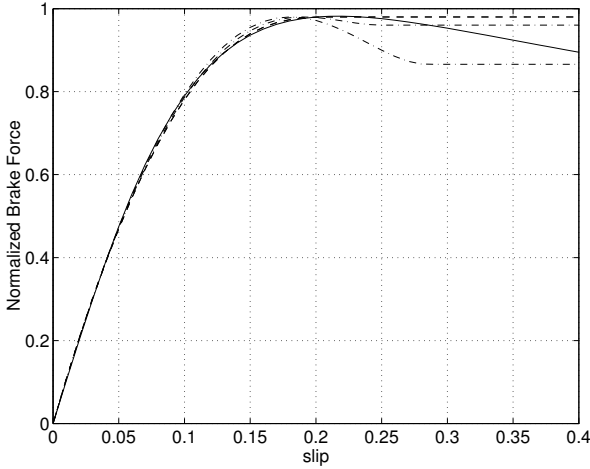
Figure 4.7 The figure shows the force-slip curve derived by the brush tire model with different friction value for adhesive and sliding areas. Solid line is the Magic Formula estimated from real data. Dashed dotted curve has $m = 1$ and dashed dotted lines has m equal to 0.6 and 0.8.

$v_{sx} = v_x\sigma_x/(1+\sigma_x)$, is done. With constant static friction the following expression is used for the kinetic friction.

$$\mu_k(\sigma_x, v) = \mu_0 - n\,v\frac{\sigma_x}{1 + \sigma_x} \tag{4.13}$$

In Figure 4.8 the brush model characteristics is shown assuming this linear velocity dependency on only μ_k and both μ_k and μ_s for two different values on n. As can be seen in the figure there is hardly any difference between using velocity dependence on the static friction or not.

Exponential Velocity Dependency

For exponential velocity dependence the following relation, proposed by C. Canudas de Wit in [Canudas de Wit *et al.*, 2001], is used

$$\mu_k(\sigma_x, v) = \mu_k + (\mu_s - \mu_k)e^{-|v\sigma_x/((1+\sigma_x)v_{st})|^\varepsilon} \tag{4.14}$$
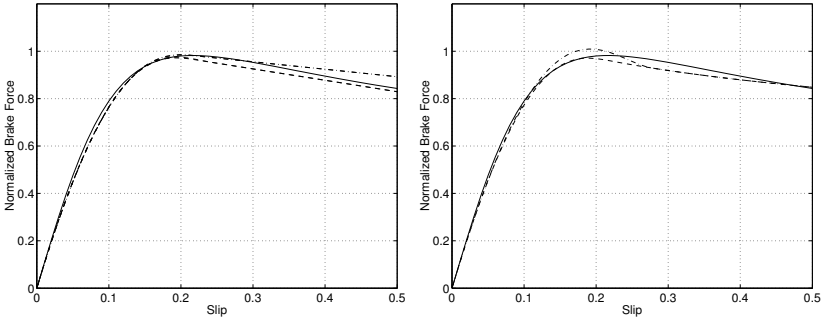
Figure 4.8 The left figure shows the force-slip relation with linear velocity dependence. Solid line is the magic formula estimated from real data. The dashed curve has $\mu_0 = 1.05$ and $n = 0.0075$ and the dashed dotted curve has $\mu_0 = 1.05$ and $n = 0.0075$. Both the case with $\mu_s = \mu_0$ and $\mu_s = \mu_k$ is plot, but the difference is hardly noticeable. To the right exponential velocity dependence is plotted for $\mu = 1.3$ and $h = 0.4$. For the dashed dotted line $\mu_s = \mu_0 = \mu_k(0)$ and the dashed $\mu_s = \mu_k(v_s)$,

Four parameters are necessary to describe this relation. It gives good flexibility and the brush model can almost be adjusted to fit any Magic Formula set. Clearly, the aim to introduce one calibration parameter is then not fulfilled and the number of parameters has to be reduced. The reduction can be done by fixing some of parameter values. In Figure 4.8 $\varepsilon = 0.5$ and $v_{st} = 30$ m/s and the calibration parameter h is introduced as

$$\mu_k(\sigma_x, v) = \mu \left(h + (1 - h)e^{-|v\sigma_x/((1+\sigma_x)30)|^{0.5}} \right) \qquad (4.15)$$

The illustration to the right in Figure 4.8 shows that the difference between the adhesive and the sliding friction gives a sharp hook on the force slip curve just before entering the slip for total sliding. When studying raw data from tests of tires this phenomenon is often observed, but it is not really covered by the Magic Formula parameterization.

Discussion

From the result in this section it can be seen that it is only possible to change the slope of the curve from the brush tire model at slip values

close to or above the point for total sliding when including velocity dependence. This is obvious considering the fact the larger slip the larger share of the brake force is depending on the friction characteristic. In some cases it has been shown that even the adhesive friction coefficient can depend on the speed that pulls the material away form its original position. This could motivate the use of equal static and kinetic friction coefficient. Assuming the case with different static and kinetic friction the slope behind the maximal force point gets too steep negative incline compared to the reference curve. This could maybe be changed by a combination of velocity dependent friction and another pressure distribution then the parabolic one. The great advantage if one could get these approximations more realistic is that it would be possible to prescribe the negative slope without or just before entering that zone.

4.3 Calibration Parameter

In the two previous subsections different ways to modify the original brush model have been described. The effect on the final force-slip relation is different depending on which of the methods that is used. Variations of the pressure distribution allows correction at slip lower than the peak force point. The velocity dependent friction mainly affects the tire model at slip values around or above the peak force depending on the choice of relation. For critical braking and ABS-situations, knowledge about the velocity dependence is useful. However, for control algorithms aiming at avoiding ABS-situations, the critical peak force and its corresponding slip value are more valuable informations. To be able to predict this point, the agreement between the model and reality is of great importance at low slip. A drawback with the introduction of asymmetric pressure distribution is that the expression gets much more complicated. However, in [Svendenius, 2003] it has been show that (4.6) can the simplified with good accuracy by Taylor expansion, as

$$F_{0x} = C_x \sigma_x + \frac{1}{3} \frac{C_x^2}{(d-1)\mu F_z} \sigma_x^2 - \frac{1}{27} \frac{(3\,d+1)C_x^3}{\mu^2\,F_z^{\,2}(d-1)^3} \sigma_x^3 + O(\sigma_x^4) \quad (4.16)$$
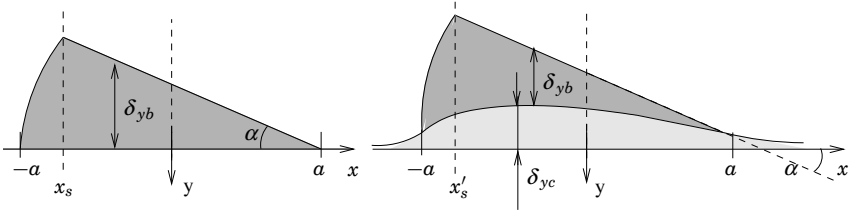
Figure 4.9 Tire lateral deformation according to the brush-model. Left: Stiff carcass. Right: Flexible carcass.

for $\sigma_x < 3\mu F_z/(C_x(1+d))$. The same approach can be applied to the formulas from the velocity dependence as well.

4.4 Carcass Flexibility

As mentioned previously the brush model described in Section 3.2 is based on the assumption of a stiff carcass. In reality the carcass is flexible and exhibits significant deformation laterally. Figure 4.9 illustrates how the carcass deformation affects the brush model. Mainly, the break-away point will move backwards and the deflection of the bristles increases differently in the contact patch. The bristles and the carcass can be seen as two spring elements connected serially, with the distinction that each bristle deflects individually, when the carcass is a coherent unit. The total deformation $\delta_y(x)$ is the sum of the bristle and carcass deflections $\delta_{yb}(x)$ and $\delta_{yc}(x)$

$$\delta_y(x) = \delta_{yb}(x) + \delta_{yc}(x) \tag{4.17}$$

and

$$dF_{yb}(x) = dF_{yc}(x) = dF_y(x) \tag{4.18}$$

Let $F_y'(\sigma_y)$ denote the lateral tire-force for a tire with flexible carcass. Regard again how the deformation of an infinitesimal bristle element at position x in the adhesive region, $\delta_y(x)$, is described by (3.9). This is a purely kinematic relation which holds also in the case of

flexible carcass. The force acting on the bristle element at x will then be

$$dF_y'(x) = c_{py}\delta_{yb}(x)\,dx = -c_{py}(\sigma_x(a-x)+\delta_c(x)) \tag{4.19}$$

when the bristle starts to slide the force is

$$dF_y'(x) = \mu dF_z(x) \tag{4.20}$$

A relation between the carcass deflection and the lateral force distribution must be established and the literature propose several ways for that. One is to treat the carcass deformation as a thread or a beam. For the thread model the force-deflection relation has the following differential form

$$S\frac{d^2\delta_c(x)}{dx^2} = q_{yc}(x) \tag{4.21}$$

where S is the tension in the thread and $q_{yc} = q_y$ is the lateral force per length unit equal to dF_y/dx. An equation system consisting of an expression for the break-away point given by the equality of (4.19) and (4.20) and one differential expression for lateral force per unit for $x_s \le x \le a$ from (4.21) and (4.19) and for $-a \le x \le x_s$ given by (4.20), can be established. The approach requires extensive calculations and will not be further treated here. It has, however, been solved and a few results is presented in [Pacejka, 1988]. A simpler approach is to assume a certain shape of the carcass deformation with an amplitude depending on the total lateral force. Here the simplest one is used, where it is assumed that the carcass still is straight, but gets a deviation towards the rolling direction. The incline is proportional to the lateral force. This is proposed in analogy with an assumption by von Schlippe discussed in [Pacejka, 2002].

$$\delta_{yc}(x) = -\frac{F_y'(\sigma_y)}{C_c}(a-x) \tag{4.22}$$

where C_c is the carcass stiffness. From (4.17), (4.22) and (3.9) it holds that

$$dF_y'(x) = c_{py}\delta_{yb}(x)\,dx = -c_{py}\left(\sigma_y - \frac{F_y'(\sigma_y)}{C_c}\right)(a-x)\,dx \tag{4.23}$$

Using (3.12) at pure lateral slip together with a parabolic pressure distribution (3.14) the position for the break-away point can be solved from

$$c_{py}\left(\sigma_y - \frac{F'_y(\sigma_y)}{C_c}\right) = \frac{3\mu_{ay}F_z}{4a^3}(a + x_s) \tag{4.24}$$

The total lateral force can be derived from the following equation

$$F'_y(\sigma_y) = \int_{x_s(F'_y(\sigma_y))}^{a} c_{py}\left(\sigma_y - \frac{F'_y(\sigma_y)}{C_c}\right)(a - x)dx + \int_{-a}^{x_s(F'_y(\sigma_y))} \mu q_z dx \tag{4.25}$$

It is realized that solving even this strongly simplified approach analytically will not render a smooth expression. Numerical solution can be easily found and a comparison between this compensation and the ordinary brush model can be seen in Figure 4.10. Some important information can, however, be derived from this model considering the effect of the flexible carcass on σ_y° , see Equation (3.17), and (3.94). Regard the case when the entire contact patch slides, i.e $x_s = a$, $\sigma_y = \sigma_y^{\circ\prime}$, and $F'_y(\sigma_y^{\circ\prime}) = \mu_{ky}F_z$. Solving (4.24) for $\sigma_y^{\circ\prime}$ under these conditions gives

$$\sigma_y^{\circ\prime} = \frac{3F_z\mu_{sy}}{2a^2 c_{py}} + \frac{\mu_{ky}F_z}{C_c} = F_z\left(\frac{3\mu_{sy}}{2a^2 c_{py}} + \frac{\mu_{ky}}{C_c}\right) \tag{4.26}$$

Next step is to derive an expression for the relation between C_c and the cornering stiffness C'_y. At very small slips $\sigma_y \approx 0$ there is no sliding in the contact patch and the tire force only consists of adhesive force. Therefore,

$$C'_y = \frac{dF'_y(\sigma_y)}{d\sigma_y}\bigg|_{\sigma_y=0} = -\frac{d}{d\sigma_y}\left(\int_{-a}^{a} c_{py}\delta_b(x)\, dx\right)\bigg|_{\sigma_y=0}$$

$$= 2a^2 c_{py}\left(1 - \frac{1}{C_c}\frac{dF'_y(\sigma_y)}{d\sigma_y}\bigg|_{\sigma_y=0}\right) = 2a^2 c_p y\left(1 - \frac{C'_y}{C_c}\right) \tag{4.27}$$

Hence, the cornering stiffness including the flexible carcass is given by

$$C'_y = \frac{C_c 2a^2 c_p y}{C_c + 2a^2 c_p y} \tag{4.28}$$

Further, the rubber will be assumed to behave isotropicly, $c_{py} = c_{px}$, which is a realistic assumption. (In Section 3.2 the carcass deformation was included in the lateral rubber stiffness.) Then the carcass stiffness can be calculated from (4.28) as

$$C_c = \frac{C_x C_y'}{C_x - C_y'} \tag{4.29}$$

where $2a^2 c_{px} = C_x$ according to (3.37). Using (4.29) then the limit-slip adjusted for carcass deformation of (4.26), $\sigma_y^{\circ\prime}$, can be written as

$$\sigma_y^{\circ\prime} = F_z \mu_y \left(\frac{2}{C_x} + \frac{1}{C_y'} \right) \tag{4.30}$$

Using $F_y^* = F_z \mu_y$, $\mu_{sy} = \mu_{ky}$, and $\hat{C}_y' = C_\alpha \cdot 180/\pi$ explains the choice of $\sigma_y^{\circ\prime}$ in (3.94).

Discussion Introducing flexibility in the carcass as described above improves the accuracy of the brush model in the lateral direction significantly, as can be seen in Figure 4.10. The approach can be used even for combined slip. The agreement for the brush model is still better in the longitudinal direction, but assuming more realistic deflections will complicate the expressions considerably. Note that this approach will not affect the main part of the self-aligning torque, M_z' and improvement of it will require more advanced carcass deflections.

4.5 Tire Dependence on Unmodeled Factors

There are a lot of factors influencing the tire behavior, and it is probably an impossible task to try to understand them all completely. It is not without reason that one of the major institute for tire testing and research (TNO, Netherlands) has derived a huge empirical equation structure to describe the tire behavior by parameter optimization. One effect that is observed in reality, but not covered by the brush model is that the braking stiffness, C_x seems to depend on the friction. A method to distinguish between different surfaces rely on this
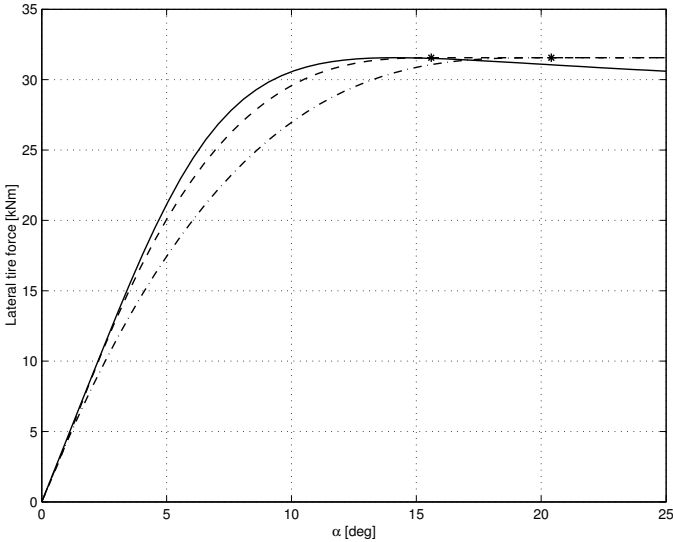
Figure 4.10 Comparison of the brush-model with (dashed) and without (dashed dotted) compensation for a flexible carcass. Asterisks denotes points for total sliding $\alpha^{\circ\prime}$ and α°. Solid line is Magic Formula empirical data given from [Gäfvert and Svendenius, 2003].

phenomena [Gustafsson, 1997]. This effect can also be seen from the measurements in Section 5.2. Another problem is the load dependence. Both the friction coefficient and the braking stiffness shows dependence on the vertical load. Experiment shows that μ is slightly decreasing for increasing load, see for instance [Nordstrom, 1983]. Also the braking stiffness depends on the load and an attempt to explain this by changes in the contact area, since $C_x = 2c_p a^2$, is done previously. Results have shown that the braking stiffness coefficient C_x/F_z decays slightly for larger vertical loads. The same holds for the cornering coefficient, with the exception that the decrease is larger. The difference is probably explained by that the carcass flexibility C_c reacts different from the bristle stiffness on load changes. Another thing that shows in this direction is that the cornering coefficient increases with inflation pressure, see [Wong, 2001], when the contact patch usu-

ally gets smaller, which results in a lower bristle stiffness. The load dependence is a very important observation and it probably has to be account for in the tiremodel since the load generally changes during the braking phase, due to load transferes.

4.6 Conclusions

This chapter has dealt with extensions to the ordinary brush-model. The effect of velocity-dependent friction has been discussed and several relations between the friction coefficient and the sliding velocity have been analyzed. Allowing an exponential decay on the friction will give a tire model that can be calibrated to measurement data in a similar way as the Magic Formula. However, many parameters are needed for that representation. Linear velocity-dependence introduces only one extra parameter, but its effect on the tire model is limited to higher slips.

The brush model is usually derived assuming symmetric pressure-distribution between the tire and the road surface and the effects of deviations from that are studied. A parameter is introduced to change the position of the center of the pressure in the contact patch, which makes it possible to adjust the tire model at low slips. It is noted that the brush model can be extended with calibration factors in different ways to increase its agreement. Since the properties at low slip are important when trying to estimate the friction coefficient by measurements in this range, which will be discussed in Section 5.3, the parameter to change the pressure distribution is particularly interesting.

The tire behavior in the lateral and longitudinal direction differs. The brush model has to be corrected for cornering due to the influence of the lateral flexibility of the carcass. It is shown that an approximation of the carcass deformation as pure twisting towards the rolling direction will improve the accuracy in this direction significantly.

5

Applications for Brake Control

An important question in this thesis is how knowledge about the tire behavior can be used in braking applications. One way is to test the tire and mathematically approximate the data to a function. Then, the function can be used to describe the tire behavior for a specific condition. This is most common for simulation purposes, but the benefit in reality depends much on the quality of the tire model. If a condition changes the vehicle stability is in danger if too much reliability is set to the tire model. The ABS-function is a good example on how knowledge about the tire characteristics in general can enhance the vehicle stability only by knowing that the wheels must not lock, since the driver then is disabled from steering the car. Another aspect which has become popular recently is to continuously estimate certain parameters so the actual tire characteristic can be predicted. Here, problems concerning sudden changes of road surfaces are major issues. This section will first discuss some of the existing methods to estimate the tire behavior. Then, the result from a vehicle test, with the aim to examine if the the brush model is valid enough to be used in this context, is presented. Finally, it is shown how the brush model can be used for estimation.

5.1 Existing Friction Estimation Methods

Much effort has been made on developing friction estimation algorithms. A literature study in this area is quite difficult, since the published articles often describe academic nice solutions, but these are often restricted to certain circumstances and with few real implementations. The company, having powerful test equipment, mostly do not publish anything due to the hard competition. One exception is a work done by NIRA-dynamics, which has been presented in many articles, i.e [Gustafsson, 1997] and also developed to a selling product. The product is an algorithm that using the wheel speed signal, the vehicle velocity and the engine torque can distinguish between the road foundations: gravel, ice, snow, and asphalt. The idea is to study changes in the wheel speed and braking stiffness. Another approach has been published in [Ray, 1997] where the speed of all wheels and the corresponding tire forces, are estimated through an extended Kalman-Busy filter and among several tire model the most probable is chosen through Bayesian learning. One method based on the brush model is published in [Pasterkamp and Pacejka, 1997]. The relation between the self-aligning torque and the lateral tire force derived by the brush model is used to estimate the friction while turning. In [Canudas de Wit *et al.*, 2001] it is shown how an observer for the friction can be achieved using the LuGre model. Many approaches uses the brush model for estimation of the friction, e.g. [Liu and Peng, 1996], [Yamazaki *et al.*, 1997], and [Pasterkamp and Pacejka, 1997]. However, no good test results are available to this approach and this section will validate the reliability of the brush model by comparisons to a vehicle test. The brush model has shown good agreement to Magic Formula optimized test data collected in laboratorial environment, see Figure 3.8. If the agreement is acceptable in real condition is another question. A method to increase the flexibility and the agreement of the brush model is to use the the calibration factor d proposed in Section 4.3 and also further discussed in [Svendenius, 2003].

5.2 Vehicle Test for Validation of the Brush Model

Test Equipment

The test was performed at the test facilities MIRA in England, where there is a separate track with different road surfaces. A special arrangement sprays water on the lane to reduce the friction. Four different foundations are available, basalt, bridport, wet and dry asphalt. The Scania test truck, with additional weight blocks mounted, is equipped with a CANSAS-measurement system to record signals from the CAN-buss with data acquisition time, 0.01s. A DGPS-sensor called V-box measures position, velocity and acceleration of the vehicle. Also a longitudinal accelerometer provides the retardation. The rotation speed of each wheel and the brake application force of each brake is measured through the brake system.

Test Procedure

Since the English security legislation around test facilities is strict the maximal speed was not higher than 40 km/h. Only the brakes at one axle are applied at the same time to reduce the number of forces working on the vehicle. The slip calculation is then also simplified, since two wheels always provides the reference speed. Three test runs were performed, each containing a number of brakings on different road surfaces. In each braking the brake pressure was applied as a ramp aiming to reach the highest possible tire force before the vehicle comes to a rest.

Signal Processing

To be able to validate the brush model the longitudinal tire force and the slip signal has to be available. None of the signals are directly measurable by the test equipment, so they have to be calculated. Since the slip calculation is sensitive for noise all signals were filtered with a second order filter, $\omega^2/(s^2 + \zeta\omega s + \omega^2)$ with $\zeta = 0.75$ and $\omega = 20$. On each side of the truck the σ-slip is derived as

$$\sigma_x = \frac{\omega_1(t) - \omega_2(t)}{\omega_2(t)} \tag{5.1}$$

where ω_1 denotes the rotation velocity of the free rolling wheel and ω_2 corresponds to the braked wheel.

It is assumed that the brake force is equal on the both sides of the truck and can be calculated by

$$F_x = \frac{ma(t)}{2} \tag{5.2}$$

The vertical force, F_z, working on each tire is also assumed to divide equal on the left and the right side. It is for the front and reap tires derived using

$$F_{zf} = \frac{mgl_2}{2l} + \frac{ma(t)h}{2l}; \quad F_{zr} = \frac{mgl_1}{2l} - \frac{ma(t)h}{2l} \tag{5.3}$$

where the negative sign is used for the rear wheels and the positive sign for the front wheels. The included parameters are given in Table 5.1. The dynamical system between the brake force application and the generation of the tire force use to be described by a first order system with a time constant depending on the wheel speed, see (2.14). The entire truck system, described by a transfer function from the tire force to the measured accelerometer signal is more complex and probably the effect of the tire dynamics is small in comparison. Therefore a first order function with a fixed time constant is assumed to describe the dynamics between the slip signal and the retardation

$$F_x = \frac{F(\sigma_x)}{Ts + 1} \tag{5.4}$$

The choice of T was done manually and affected the result considerably. The value that gave the brush model best agreement, $T = 0.2$ s was used for the calculations.

Result and Validation

In Figure 5.1 the results from a number of brakings are shown. The two figures show results from two different test runs, where only braking with the front wheel brakes are performed. The first collection includes braking on different surfaces and the second only on wet asphalt. The normalized brake force is plotted against the wheel slip and

Table 5.1   Vehicle parameters. (CoG: Center of gravity)

Parameter	Value	Significance
m	12412 kg	Mass of vehicle
l	3.8 m	Length of wheel base
l_1	1.97 m	Distance between front axle and CoG
h	0.85 m	Height of Cog

Table 5.2   Surface friction values compared to parameters from the brush model optimized to the measurements.

Road surface	μ	$\hat{\mu}$	$\hat{C}_x$	$\lambda°$
Basalt	0.10 - 0.15	0.125	13	0.030
Bridport	0.3 - 0.4	0.4	20	0.064
Wet Asphalt	0.65 - 0.80	0.77	23	0.11
Dry Asphalt	0.80 - 0.90			

compared to brush model approximations. The difference between the road foundations is clearly visible. The result also follows the brush model very tightly and the optimized parameters from Equation (4.1) are presented in Table 5.2. The predicted friction values are realistic compared to the nominal values. This means that the result from the modeling in Section 3.2 agrees well to real circumstances (restricted to longitudinal motions), even though it is strongly simplified. The measurements also show good repetivity, which is clear from the brakings on asphalt. Some of the spread between the collections can still be explained by different amount of water on the road. The reason for lack of data from brakings on dry asphalt is obvious since the test was performed in England. An uncertainty in the test is the dynamic relation between the force and slip measurements, since the slip is measured at the wheel rim and the force is derived from retardation of the vehicle.
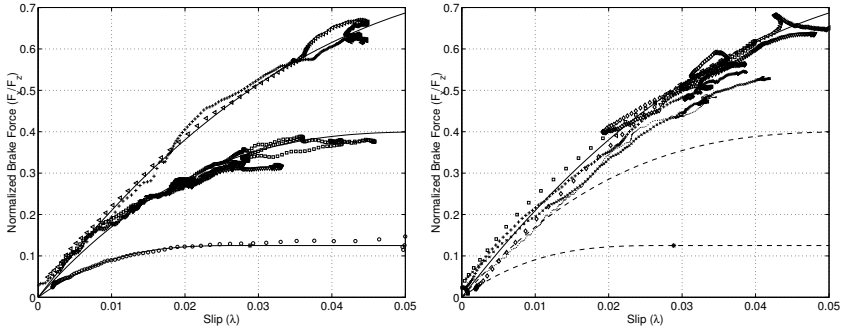
Figure 5.1   Plot illustrating the braking force as a function of the slip, λ. Measurement values are dotted and the solid line is the brush-model approximation. Left: Test run no. 1. Right: Test run no. 2 (only asphalt).

5.3 Friction Estimation Using the Brush Model

The expression for the brush model including a suitable d-factor, given by (4.16), is well suited for friction estimation since the two parameters, C_x, and μ are explicitly included. The brush model can be written on the following form

$$y = \theta_0 u_0 + \theta_1 u_1 + \theta_2 u_2 + e \tag{5.5}$$

with the following regressors

$$y = F_x \tag{5.6}$$

$$u_0 = C_{x0}\sigma_x \tag{5.7}$$

$$u_1 = -\frac{1}{3\mu_0}\frac{(C_{x0}\sigma_x)^2}{F_z} \tag{5.8}$$

$$u_2 = \frac{1}{27\mu_0^2}\frac{(C_{x0}\sigma)^3}{F_z^2}\frac{3d+1}{(d-1)^3} = \frac{u_1^2}{3u_0}\frac{3d+1}{d-1} \tag{5.9}$$

The tire parameters of interest can be derived as

$$\hat{C}_x = \theta_0 C_{x0} \tag{5.10}$$

$$\hat{\mu} = \frac{\theta_0^2}{\theta_1}\mu_0 \tag{5.11}$$

Then the third parameter θ_2 can be expressed by the other two parameters θ_0 and θ_1 as $\theta_2 = \theta_1^2/\theta_0$ and (5.5) can be rewritten in the following form

$$y = \theta_0 u_0 + \theta_1 u_1 + \frac{\theta_1^2}{\theta_0}\frac{u_1^2}{3\,u_0}\frac{3d+1}{d-1} + e \tag{5.12}$$

There exists a number of estimation schemes to treat this kind of model structure. A lot of criteras have to be set concerning the update rate of the parameters before an algorithm can be chosen or derived. There is also an enormous work to be done to tune parameters and gains. Further measurements to exactly reveal the noise ratio on the signals are necessary. This is hopefully, a good challenge for future work.

6

Conclusions and Future Work

6.1 Conclusions

This thesis has mainly two aims. The first is to gain knowledge and understanding about how a tire transmits the force from the rim to the road. This has been done by studying existing methods to physically model the tire-road interaction. The modeling has been aimed at understanding and also been kept as simple as possible. As a base the brush model theory has been used. The influence of additional factors such as velocity and wheel load has been studied and discussed, even though some of the effects, seen in measurements not have been covered by the modeling. The coupling between the longitudinal and lateral tire force has been discussed in detail and a new proposal to derive the combined slip forces from pure slip models has been presented. This method relies on the physics from the brush model and includes a velocity dependency which is derived from the pure slip models. All information is derived from the models which allows continuous changes of the tire characteristics.

The second aim is to examine how the knowledge about the tire behavior can be used in braking applications. The dynamics of the tire is one effect that has to be accounted for since the forces and movements in the contact patch are of interest, but the measurement now days

are limited to the rim. Basic equations for this has been presented and the accuracy needed will be determined from further testing. A theory for how the brush model can be used for detection of road surface has also been discussed. In this matter the accuracy of the brush model is an important issue and a method to calibrate it by introducing an extra factor is also discussed. Results from a vehicle test have been presented which shows good agreement between the brush model and tire behavior in real conditions. This shows that the accuracy of the brush model seems to be sufficient for surface prediction.

6.2 Future Work

The future work will sprawl out in two directions. The brush model seems to agree well with observations from vehicle tests and its structure can probably be used for friction estimation. However, to create a reliable estimation algorithm that can handle non-equally spaced measurements, adopt slowly for wear and tire changes, and rapidly detect a sudden friction loss, will require a lot of mathematical work. On the other hand there are a lot of practical problems to deal with. The treatment of non-modeled factors as the load dependency and friction sensitivity in the braking stiffness is one example. Another is the implementation and verification of the dynamic relation between the measured brake force and the force in the contact patch. This requires more vehicle testing and further development of the existing measuring equipment.

7

Bibliography

Bakker, E., L. Nyborg, and H. B. Pacejka (1987): "Tyre modelling for use in vehicle dynamics studies." SAE Technical Paper 870421.

Bakker, E., H. B. Pacejka, and L. Lidner (1989): "A new tire model with an application in vehicle dynamics studies." SAE Technical Paper 890087.

Bayle, P., J. F. Forissier, and S. Lafon (1993): "A new tire model for vehicle dynamics simulations." *Automotive Technology International*, pp. 193–198.

Böhm, F. and H.-P. Willumeit, Eds. (1996): *Tyre Models for Vehicle Dynamics Analysis*. Swets & Zeitlinger Publishers. Supplement to Vehicle System Dynamics Volume 27.

Brach, R. M. and R. M. Brach (2000): "Modeling combined braking and steering tire forces." SAE Technical Paper 2000-01-0357.

Canudas de Wit, C. and P. Tsiotras (1999): "Dynamic tire friction models for vehicle traction control." In *Proceedings of the 38th IEEE Conference on Decision and Control*, vol. 4, pp. 3746–3751.

Canudas de Wit, C., P. Tsiotras, and X. Claeys (2001): "Friction tire/road modeling, estimation and optimal braking control." In *Lund NACO2 Workshop*.

Continental (2003): "History of passenger tire." Internet. http://www.conti-online.com/.

Deur, J. (2002): "A brush-type dynamic tire friction model for non-uniform normal pressure distribution." In *Proceedings of the 15th Triennial IFAC World Congress*. Barcelona, Spain.

Ellis, J. R. (1994): *Vehicle Handling Dynamics*. Mechanical Engineering Publications Limited, London.

Gäfvert, M. and J. Svendenius (2003): "Construction of semi-empirical tire models for combined slip." Technical Report ISRN LUTFD2/TFRT--7606--SE. Department of Automatic Control, Lund Institute of Technology, Sweden.

Gim, G. and P. E. Nikravesh (1991): "An analytical model of pneumatic tyres for vehicle dynamics simulations. part 2: Comprehensive slips." *International Journal of Vehicle Design*, **12:1**, pp. 19–39.

Goyal, S. (1989): *Planar Sliding Of A Rigid Body With Dry Friction: Limit Surfaces And Dynamics Of Motion*. PhD thesis, Cornell University, Department Of Mechanical Engineering.

Gustafsson, F. (1997): "Slip-based tire-road friction estimation." *Automatica*, **33:6**, pp. 1087–1099.

ISO 8855 (1991): "Road vehicles — Vehicle dynamics and road-holding ability — Vocabulary."

Kiencke, U. and L. Nielsen (2000): *Automotive Control Systems: For Engine, Driveline, and Vehicle*. Springer-Verlag.

Liu, C.-S. and H. Peng (1996): "Road friction coefficient estimation for vehicle path prediction." *Vehicle system Dynamics*, **25**, pp. 413–425.

Michelin (2003): "Michelin's group site." Internet. http://www. michelin.com/.

Nguyen, P. K. and E. R. Case (1975): "Tire friction models and their effect on simulated vehicle dynamics." In *Proceedings of a Symposium on Commercial Vehicle Braking and Handling*, number UM-HSRI-PF-75-6, pp. 245–312.

Nicholas, V. T. and T. Comstock (1972): "Predicting directional behavior of tractor semitrailers when wheel anti-skid brake systems are used." In *ASME Winter Annual Meeting*, number Paper No. 72–WA/Aut-16.

Nielsen, L. and L. Eriksson (1999): "Course material vehicular systems.". Linköping Institute of Technology, Vehicular Systems, ISY.

Nordstrom, O. (1983): *Antilås system för tungafordon, VTI Rapport nr 257*. Klintland grafiska.

NWT-Consortium (2002): "Tire tech 101." Technical Report. North West Transportation Consortium.

Olsson, H. (1996): *Control Systems with Friction*. PhD thesis ISRN LUTFD2/TFRT--1045--SE, Department of Automatic Control, Lund Institute of Technology, Sweden.

Pacejka, H. B. (1988): "Modelling of the pneumatic tyre and its impact on vehicle dynamic behavior." Technical Report i72B. Technische Universiteit Delft.

Pacejka, H. B. (2002): *Tyre and Vehicle Dynamics*. Butterworth-Heinemann.

Pasterkamp, W. R. and H. B. Pacejka (1997): "The tyre as a sensor to estimate friction." *Vehicle System Dynamics*, **27**.

Pauwelussen, J. P., G. Anghelache, C. Theodorescu, and A. Schmeitz (1999): *European Tyre School*, chapter 10 — Truck tyre behavior in use and testing methods. Nokian Tyres plc. http://www.tut.fi/plastics/tyreschool.

Pottinger, M. G., W. Pelz, and G. Falciola (1998): "Effectiveness of the slip circle: "COMBINATOR", model for combine tire cornering and braking forces when applied to a range of tires." SAE Techical Paper 982747.

Ray, L. (1997): "Nonlinear tire force estimation and road friction identification: Simulation and experiments." *Automatica*, **33:10**, pp. 1819–1833.

SAE Recommended Practice J670e (1976): "Vehicle dynamics terminology."

Schuring, D. J., W. Pelz, and M. G. Pottinger (1996): "A model for combined tire cornering and braking forces." In *Investigations and Analysis in Vehicle Dynamics and Simulation*, pp. 61–83. SAE International. SAE Technical Paper 960180.

Svendenius, J. (2003): "Wheel model review and friction estimation." Technical Report ISRN LUTFD2/TFRT—7607–SE. Department of Automatic Control, LTH, Sweden.

Thomson, J. (2003): "What we should know about tires." Internet. http://www.jags.org/TechInfo/2001/05May/tires.

Thorvald, B. (1998): *On truck tyre modelling*. PhD thesis ISRN LUTFD2/TFRT--KTH/FKT/DA–98/29–SE--SE, KTH.

Velenis, E., P. Tsiotras, and C. C. de Wit (2002): "Extension of the lugre dynamic tire friction model to 2d motion." In *Mediterranean Conference on Control and Automation (MED2002)*, vol. 10th.

Wong, J. Y. (2001): *Theory of Ground Vehicles*, 3 edition. John Wiley & Sons.

Yamazaki, S., O. Furukawa, and T. Suzuki (1997): "Study on real time estimation of tire to road friction." *Vehicle System Dynamics*, **27**.